Cell Reports Physical Science, Volume *2*

Supplemental information

Topology and ground state control in open-shell donor-acceptor conjugated polymers

Kevin S. Mayer, Daniel J. Adams, Naresh Eedugurala, Molly M. Lockart, Paramasivam Mahalingavelar, Lifeng Huang, Luke A. Galuska, Eric R. King, Xiaodan Gu, Michael K. Bowman, and Jason D. Azoulay

Supplemental Experimental Procedures

1. General remarks

All manipulations of air and/or moisture sensitive compounds were performed under an inert atmosphere using standard glovebox and Schlenk techniques. Reagents, unless otherwise specified, were purchased from Sigma-Aldrich and used without further purification. 1,1,2,2-Tetrachloroethane-d_2 and chloroform-*d* were purchased from Cambridge Isotope Laboratories and used as received. Tetrakis(triphenylphosphine)palladium(0) ($Pd(PPh_3)_4$) and aluminum trichloride ($AlCl_3$) were purchased from Strem Chemicals and used as received. (4,4-dimethyl-4*H*-cyclopenta[2,1-*b*:3,4-*b*′]dithiophene-2,6-diyl)bis(trimethylstannane) (**M1**),[1] dithieno[3,2-*b*:2′,3′-*d*]thiophene (DTT), 2,6-bis(trimethylstannyl)dithieno[3,2-*b*:2′,3′-*d*]thiophene (**M2**),[2] 4,7-dibromobenzo[*c*][1,2,5]thiadiazole-5,6-diamine,[3] 2-hexadecylthiophene[4] were prepared according to literature procedures.

^1H and ^{13}C NMR spectra were collected on a Bruker Avance III 600 MHz spectrometer and chemical shifts, δ (ppm) were referenced to the residual solvent impurity peak of the solvent. Data are reported as: s = singlet, d = doublet, t = triplet, m = multiplet, br = broad, and coupling constant, (*J*) are reported in Hz. Flash chromatography was performed on a Teledyne Isco CombiFlash Purification System using Redi*Sep* Rf prepacked columns. Microwave assisted reactions were performed in a CEM Discover SP microwave reactor. The number average molecular weight (M_n) and dispersity (*Đ*) were determined by gel permeation chromatography (GPC) using a universal calibration method at 160 °C in 1,2,4-trichlorobenzene (stabilized with 125 ppm of BHT) in an Agilent PL-GPC 220 high temperature GPC/SEC system using a set of three PLgel 13 µm Olexis columns. Polymer samples were dissolved at a concentration of 1–2 mg mL^{-1} in 1,2,4-trichlorobenzene with stirring for 4 hours at 160 °C.

2. Synthesis

1,2-bis(5-hexadecylthiophen-2-yl)ethane-1,2-dione (1). Anhydrous methylene chloride (50 mL) was added to $AlCl_3$ (8.17 g, 61.3 mmol) under a nitrogen atmosphere and stirred to fully disperse the contents. The mixture was then cooled to –10 °C. Oxalyl chloride (1.74 g, 13.7 mmol) was added dropwise. After addition, the mixture was stirred for an additional 20 minutes and a solution of 2-hexadecylthiophene (9.0 g, 29.2 mmol) and pyridine (2.13 g, 27.0 mmol) in methylene chloride (15 mL) was added dropwise using an addition funnel. The reaction mixture was allowed to slowly warm to room temperature. After reaching room temperature, the reaction was quenched with ice, resulting in precipitation of a solid material. The solid precipitate was collected by vacuum filtration and recrystallized from 2-propanol affording 17.22 g of a yellow crystalline solid (25.66 mmol, 88%). Data are as follows: ^1H NMR (600 MHz, chloroform-*d*): δ 7.86 (d, *J* = 3.8 Hz, 2H), 6.88 (d, *J* = 3.8 Hz, 2H), 2.88 (t, *J* = 7.6 Hz, 4H), 1.72 (p, *J* = 7.6 Hz, 4H), 1.37 (br, 4H), 1.26 (br, 48H), 0.88 (t, *J* = 7.0 Hz, 6H). ^{13}C NMR (151 MHz, chloroform-*d*) δ 182.73, 160.18, 137.87, 136.68, 126.53, 32.08, 31.43, 30.98, 29.83, 29.64, 29.51, 29.43, 29.19, 22.84, 14.25. Mass spectrometry (MS) [electrospray ionization (ESI)] exact mass calculated for $C_{42}H_{70}O_2S_2$ is as follows: m/z 671.4890 ($[M^+]$ + $[H^+]$) and 671.4884 (found).

4,9-dibromo-6,7-bis(5-hexadecylthiophen-2-yl)-[1,2,5]thiadiazolo[3,4-*g*]quinoxaline (TQBr$_2$). 1,2-bis(5-hexadecylthiophen-2-yl)ethane-1,2-dione (**1**) (1.24 g, 1.85 mmol), 4,7-dibromobenzo[*c*][1,2,5]thiadiazole-5,6-diamine (1.20 g, 3.70 mmol) and 80 mL of an acetic acid:chloroform solution (5:1) were combined in a Schlenk flask equipped with a stir bar. The mixture was vigorously purged with nitrogen for 5 minutes and then sealed. The mixture was heated to 70 °C and stirred over the course of 5 days. After cooling to room temperature, the mixture was poured into methanol (15 mL). The resulting precipitate was collected by vacuum filtration and residual solvents were removed *in vacuo*. Purification by flash chromatography using a hexanes:methylene chloride solution (20:1) gave 613 mg of red solid (0.639 mmol, 35%). Data are as follows: ^1H NMR (600 MHz, chloroform-*d*): δ 7.53 (d, *J* = 3.8 Hz, 2H), 6.76 (d, *J* = 3.8 Hz, 2H), 2.90 (t, *J* = 7.7 Hz, 4H), 1.78 (p, *J* = 7.6 Hz, 4H), 1.43 (br, 4H), 1.36 (s, 4H), 1.26 (br, 44H), 0.88 (t, *J* = 6.9 Hz, 6H). ^{13}C NMR (151 MHz, chloroform-*d*) δ 154.52, 152.43, 148.97, 139.01, 137.86, 132.54, 125.44, 112.62, 32.08, 31.62, 30.81, 29.85, 29.82, 29.80, 29.71, 29.50, 29.38, 22.84, 14.26. Mass spectrometry (MS) [electrospray ionization (ESI)] exact mass calculated for $C_{48}H_{70}Br_2N_4S_3$ is as follows: m/z 957.3208 ($[M^+]$ + $[H^+]$) and 957.3211 (found).

Poly(4-(4,4-dimethyl-4*H*-cyclopenta[2,1-*b*:3,4-*b*′]dithiophen-2-yl)-6,7-bis(5-hexadecylthiophen-2-yl)-[1,2,5]thiadiazolo[3,4-*g*]quinoxaline) (P1). A microwave tube was charged with **M1** (0.106 mmol, 1.05 equiv.) and **TQBr$_2$** (0.101 mmol, 1.00 equiv.) The tube was brought inside a nitrogen filled glovebox, and 400 µL of a $Pd(PPh_3)_4$/xylenes stock solution (3.50 mol %) was added followed by an additional 400 µL

xylenes. The tube was sealed and subjected to the following reaction conditions in a microwave reactor with stirring: 120 °C for 5 minutes, 140 °C for 5 minutes, and 170 °C for 30 minutes. After this time, the reaction was allowed to cool, leaving a solid gelled material. The mixture was precipitated into methanol and collected via filtration. The residual solid was loaded into an extraction thimble and washed successively (under a nitrogen atmosphere and in the absence of light) with methanol (2 hours), acetone (2 hours), hexanes (2 hours), a 1:4 mixture of hexanes and tetrahydrofuran (12 hours), and then acetone (2 hours). The polymer was dried *in vacuo* to give 78.3 mg (54 %) of a black solid. Data are as follows: M_n = 14.2 kg mol^{-1} and $Đ$ = 2.24; ^{1}H NMR (600 MHz, 1,1,2,2-tetrachloroethane-d_2, 413 K): δ 9.14–6.93 (br, 6H), 3.07 (br, 4H), 1.95 (br, 10H), 1.34 (br, 52H), 0.95 (br, 6H).

Poly(4-(4,4-dimethyl-4H-cyclopenta[2,1-*b*:3,4-*b*′]dithiophen-2-yl)-6,7-bis(5-hexadecylthiophen-2-yl)-[1,2,5]thiadiazolo[3,4-*g*]quinoxaline) (P2). A microwave tube was charged with **M2** (0.0657 mmol, 1.05 equiv.) and **TQBr$_2$** (0.0626 mmol, 1.00 equiv.) The tube was brought inside a nitrogen filled glovebox, and 300 µL of a Pd(PPh$_3$)$_4$/xylenes stock solution (3.50 mol %) was added followed by 250 µL xylenes. The tube was sealed and subjected to the following reaction conditions in a microwave reactor with stirring: 120 °C for 5 minutes, 140 °C for 5 minutes, and 170 °C for 45 minutes. After this time, the reaction was allowed to cool, leaving a solid gelled material. The mixture was precipitated into methanol and collected via filtration. The residual solid was loaded into an extraction thimble and washed successively (under a nitrogen atmosphere and in the absence of light) with methanol (2 hours), acetone (2 hours), hexanes (2 hours), a 1:5 mixture of hexanes and tetrahydrofuran (12 hours), and then acetone (2 hours). The polymer was dried *in vacuo* to give 66.3 mg (46%) of a black solid. Data are as follows: M_n = 30.5 kg mol^{-1} and $Đ$ = 1.91; ^{1}H NMR (600 MHz, 1,1,2,2-tetrachloroethane-d_2, 413 K): δ 7.80–7.03 (br, 6H), 3.12 (br, 4H), 1.38 (br, 4H), 1.34 (br, 52H), 0.97 (br, 6H).

3. Experimental section

3.1. UV–vis–NIR and Fourier transform infrared spectroscopy

UV–vis–NIR and Fourier transform infrared (FTIR) spectra were recorded from 0.375 to 3.30 µm and from 3.30 to 16.40 µm using a Cary 5000 UV–vis–NIR spectrophotometer and Bruker VERTEX 80 FTIR spectrometer, respectively. Thin films were prepared by spin coating a chlorobenzene solution (10 mg mL^{-1}) onto quartz or NaCl substrates at 1,000 rpm. Solution spectra were recorded from 0.375 to 3.30 µm in chlorobenzene.

3.2. Electrochemistry

Electrochemical characteristics were determined by cyclic voltammetry (50 mV s^{-1}) carried out on drop-cast polymer films at room temperature in degassed anhydrous acetonitrile with tetrabutylammonium hexafluorophosphate (0.1 M) as the supporting electrolyte. The working electrode was a platinum wire, the counter electrode was a platinum wire and the reference electrode was Ag/AgCl. After each measurement the reference electrode was calibrated with ferrocene and the potential axis was corrected to the normal hydrogen electrode (NHE) using −4.75 eV for NHE.[5] The highest occupied molecular orbital energy level (E_{HOMO}) was estimated as −4.41 eV and −4.86 eV from the onset of oxidation for **P1** and **P2**, and lowest unoccupied molecular orbital energy level (E_{LUMO}) estimated as −4.03 eV and −4.10 eV from the onset of reduction of the third scan for **P1** and **P2**. The electrochemical band gap was calculated as 0.38 eV and 0.76 eV from the difference between E_{HOMO} and E_{LUMO} for **P1** and **P2**.

3.3. Conductivity and charge transport measurements

The conductivity and organic field-effect transistor (OFET) characteristics were evaluated using a typical bottom-gate, bottom-contact geometry. Silicon substrates were cleaned sequentially using 2% Hellmanex detergent in DI water, DI water, acetone, and isopropyl alcohol for 10 min each using sonication and then dried in an oven. The substrates were then treated in a UV/ozone cleaner for 20 min. The heavily n-doped silicon substrates with a 300 nm thermally grown SiO_2 dielectric were prepared as the bottom-gate electrode. The SiO_2 dielectric was passivated with octadecyltrichlorosilane ($CH_3(CH_2)_{17}SiCl_3$). 5 nm of chromium was thermally evaporated as an adhesive layer followed by 60 nm of gold at 10^{-6} torr using a shadow mask. The defined channel width was 1 mm, and the channel length was 30 µm. A 10 mg mL^{-1} polymer solution was spin coated onto the substrate with pre-patterned Au electrodes at 1000 rpm for 60 s.

Devices were tested on a probe station (Signatone 1160 series) inside a nitrogen filled glovebox, and the data were recorded on a Keithley 4200 semiconductor characterization system. The conductivity measurements were conducted using a two-point probe method (source and drain, without gate) by sweeping the voltage from –2 to 2 V. The conductivity was determined from the equation (S1):

$$\sigma = \frac{I}{V} \times \frac{L}{WT} \quad \text{(Eq. S1)}$$

where σ, I, V, L, W, and T represent conductivity, current, voltage, channel length, channel width, and polymer layer thickness (measured by AFM), respectively.[5] The hole mobility was extracted from the linear region of the transfer curve in a transistor geometry based on the equation (S2):

$$\mu = \frac{L}{WC_{\mathrm{i}}V_{\mathrm{D}}} \frac{\Delta I_{\mathrm{D}}}{\Delta V_{\mathrm{G}}} \quad \text{(Eq. S2)}$$

where μ, L, W, C_{i}, V_{D}, I_{D}, and V_{G} represent the mobility, channel length, channel width, capacitance of the dielectric layer (300 nm thick SiO_2 layer), drain voltage, drain current, and gate voltage, respectively.[5]

3.4. Grazing-incidence wide-angle x-ray scattering (GIWAXS)

GIWAXS was performed using a Xenocs Xeuss 2.0 SAXS/WAXS lab source instrument. Each sample was prepared by spin-coating a film from chlorobenzene onto a Si wafer (as previously described). Films were dried and used after casting or thermally annealed at 125°C for 10 minutes. Samples were exposed for 2 hours, under a vacuum environment, with an incident beam energy of 8.05 keV and a beam geometry of 1.2 × 1.2 mm^2. The sample-to-detector distance was approximately 157 mm as determined via a silver behenate standard. Data processing was performed using WaveMetrics Igor Pro with Nika script and WAXStools software. Line-cuts were utilized to assess both in-plane and out-of-plane scattering.

3.5. Electron paramagnetic resonance (EPR) spectroscopy

Room temperature continuous-wave EPR spectra were recorded on a Bruker EMXmicro EPR spectrometer operating in the X-band. Solid-state samples were loaded into 4 mm quartz tubes and evacuated to 40 mbar for 12 hours before flame sealing under vacuum. Spin concentration was obtained by comparing solid-state samples against a 2,2-diphenyl-1-picrylhydrazyl standard with a known spin concentration. EPR measurements of solid samples stored at room temperature under a nitrogen atmosphere showed no discernable changes over a period of two weeks (Figure S31). Solution samples were prepared from diluting a stock polymer solution in chlorobenzene to 0.4 mg mL^{-1} (~10^{-5} M) and sealed in the quartz tube in a nitrogen filled glovebox. Variable-temperature measurements were performed on a Bruker E540 or E680 EPR spectrometer operating at the X-band. The EPR signal intensity from 20 to 5 K was utilized to extract the singlet–triplet energy splitting (ΔE_{ST}) through fitting the data to the Bleaney–Bowers equation[6] (S3):

$$I_{\mathrm{EPR}} = \frac{C}{T} \frac{3e^{-2J/k_{\mathrm{B}}T}}{1+3e^{-2J/k_{\mathrm{B}}T}} \quad \text{(Eq. S3)}$$

where C is a constant, k_{B} is the Boltzmann constant, J is the intramolecular exchange coupling constant, and $2J$ is ΔE_{ST}. A dilute solution (0.4 mg mL^{-1}) was used to elucidate the single-chain behavior. The fit parameters ΔE_{ST} = 7.10 × 10^{-3} and –5.24 kcal mol^{-1} were obtained for **P1** and **P2**.

In the two-pulse spin echo experiment, the two-pulse Hahn echo sequence was used (π/2-τ-π-τ-echo) and the intensity of the echo was measured as a function of τ for different microwave powers at 5 K on a solid-state sample. The fractal dimensionality (d) for the spatial distribution of electron spins for **P1** was determined from these two-pulse spin echo measurements of instantaneous diffusion by fitting the ratio of the spin echo decays at the two-pulse powers differing by 6 dB with the equation (S4):

$$\ln[V_1(\tau)/V_2(\tau)] = a_0 - k\tau^{(d/3)} \quad \text{(Eq. S4)}$$

where V_1 and V_2 represent the echo measured at different microwave powers, 8 and 14 dB respectively, τ is the inter-pulse delay, and a_0, k, d are fit parameters. The fit revealed that d is approximately equal to 1 (0.75) for the solid-state sample. This form of pulse dipolar spectroscopy indicates that the density of spins $f(r)dr$ increases linearly with the distance r for the first several nanometers.[7]

3.6. Superconducting quantum interference device (SQUID) magnetometry

Magnetometry data was collected using the Quantum Design MPMS3-SQUID VSM by loading the powder samples into polycarbonate capsules from Quantum Design and suspending the capsules in straws, also from Quantum Design. For the magnetization as a function of temperature measurements, the magnetic moment was recording upon warming after cooling in zero-magnetic-field, after allowing the sample to reach thermal equilibrium (approximately 10 minutes) at low temperature. For the magnetization as a function of field isotherms, the magnetic moment was recording after allowing the sample to reach thermal equilibrium, beginning from high field, ramping down incrementally and allowing the field to stabilize at each step before recording. Background of the straw and capsule was recorded and accounted for. In Figure S8B and C, we plot the signal from the sample together with the background measurement to highlight the relative intensity of the sample signal to the weak background signal. Considering the strength of the magnetic moment of the sample, it is not surprising that the original curve is largely unaffected by background subtraction. It is also important to note that these data show the raw signal and therefore have not undergone an adjustment of the diamagnetic component of the polymer which is inherently present. Magnetization data was collected over the range of T = 2 – 375 K with applied field H = 1 kOe. The descending magnetization curve at 5, 6, and 7 K was measured from H = 70 kOe to 0 kOe to facilitate comparisons between the range of temperatures for which **P1** EPR data was collected.

3.6.1. Curie–Weiss fitting

The Curie-Weiss function of equation (S5) can be derived beginning from the Hamiltonian of a magnetic moment μ in a magnetic field B,

$$\hat{\mathrm{H}} = -\boldsymbol{\mu} \cdot \mathbf{B}$$

From here, the Curie Law can be found as,

$$M = \frac{CH}{T} \rightarrow \chi = \frac{C}{T}$$

where $\chi = \frac{M}{H}$ and in the general case $C = \frac{Ng^2 J(J+1)\mu_{\mathrm{B}}^2 \mu_0}{3k_{\mathrm{B}}}$, where N is the number of magnetic moments, J is the total angular momentum, μ_B is the Bohr magneton, and μ_0 is the permeability of free space.
If we consider interaction between magnetic moments and define the field due to neighbors as $N_{\mathrm{W}}M$, the magnetization becomes $M = \frac{C\left(H + N_{\mathrm{W}}M\right)}{T} = \frac{CH}{T - CN_{\mathrm{W}}}$ and the susceptibility is found as the Curie-Weiss Law,

$$\chi = \frac{C}{T - \theta} \qquad \text{(Eq. S5)}$$

3.6.2. Brillouin fitting

The Brillouin function of equation (S7) can be derived beginning from the Hamiltonian of a magnetic moment μ in a magnetic field B,

$$\hat{\mathrm{H}} = -\boldsymbol{\mu} \cdot \mathbf{B}$$

The final form used here is found by taking the derivative of free energy with respect to the field, simplifying, and letting $J \rightarrow S$ and $B \rightarrow H$.

$$\frac{M}{M_{sat}} = \frac{2S+1}{2S}\coth\left(\frac{2S+1}{2S}\frac{gS\mu_{\mathrm{B}}}{k_{\mathrm{B}}}x\right) - \frac{1}{2S}\coth\left(\frac{1}{2S}\frac{gS\mu_{\mathrm{B}}}{k_{\mathrm{B}}}x\right) \qquad \text{(Eq. S6)}$$

where the parameter x is defined as $x = H/T$, H is the field in Oersted and T is the temperature, g is the g-factor, k_{B} is the Boltzmann constant, M_{sat} is the saturation magnetization, μ_{B} is the Bohr magneton and S, the spin quantum number, is the fitting parameter.

3.6.3. Bleaney–Bowers fitting

The Bleaney-Bowers equation (S6) is derived for two magnetically coupled S = ½ centers. The general exchange Hamiltonian is:

$$\hat{\mathrm{H}} = -2J(\mathbf{S}_1 \cdot \mathbf{S}_2)$$

The final form of the Bleaney-Bowers equation results from simplifications of the Van Vleck equation and is found to be:

$$\chi = \frac{N_\mathrm{A}\mu_\mathrm{B}^2 g^2}{kT}\frac{2e^{2J/k_\mathrm{B}T}}{1+3e^{2J/k_\mathrm{B}T}} \qquad \text{(Eq. S7)}$$

where N_A is Avogadro's number, μ_B is the Bohr magneton, g is the g-factor, k is the Boltzmann constant, and the fit parameter is the temperature T.[8]

3.7. Thermogravimetric Analysis (TGA)

TGA was conducted on a TA Instruments Q500 thermogravimetric analyzer by heating from room temperature to 800° at a heating rate of 10°C min^{-1} under a N_2 flow of 40 mL min^{-1}. The polymers displayed good thermal stability with 1% degradation at approximately 360.2 °C for **P1** and 251.8 °C for **P2** and 5% at approximately 424.7 °C for **P1** and 360.2 °C for **P2** (Figure S30).

3.8. Doping Study

Thin films were prepared by spin-coating a chlorobenzene solution (10 mg mL^{-1}) onto quartz substrates at 800 rpm for 60 s. The pristine thin-film absorption spectrum was recorded as a reference. The solutions were heated at 60 °C for 2 hours and spin-coated onto quartz substrates at 800 rpm for 60 s. In the sequential doping study, 0.25 mL of a 2,3,5,6-tetrafluoro-7,7,8,8-tetracyano-quinodimethane (F4TCNQ) solution in acetonitrile (concentration: 5, 10, 50, and 100 ppm) was applied to the film, equilibrated (20 s), and the excess solution was removed by spin-coating at 800 rpm for 60 s. The absorption spectrum was recorded, and the experiment repeated via the iterative deposition of F4TCNQ solutions with different concentrations onto the same film. We also reacted the polymer with hydrazine by combining 78 µL of hydrazine solution (1.0 M in THF) with 0.5 mL of a polymer solution of **P1** and **P2** (10 mg mL^{-1} in chlorobenzene). After stirring for 2 hours, the solution was spin-coated onto quartz substrates at 800 rpm for 60 s yielding an identical absorption spectrum. The experiment was repeated with new films to include the sequential doping with 0.25 mL of the free radical form of 2,6-Di-tert-butyl-α-(3,5-di-tert-butyl-4-oxo-2,5-cyclohexadien-1-ylidene)-p-tolyloxy (galvinoxyl). Acetonitrile solutions (concentration: 6, 12, 18, and 24 ppm) were applied to the film, equilibrated for 20 s, and excess removed by spin-coating at 800 rpm for 60 s. The absorption spectrum was recorded, and the experiment repeated via the iterative deposition of galvinoxyl solutions with different concentrations onto the same film. This was repeated again with new films to include the sequential doping with 0.25 mL of hydrochloric acid (HCl) in water (concentration: 0.5, 1.0, 1.5, 2.0, and 2.5 M) applied to the film, equilibrated (20 s), and excess solution removed by spin-coating at 800 rpm for 60 s. The absorption spectrum was recorded, and the experiment repeated via the iterative deposition of HCl solutions with different concentrations onto the same film.

3.9. Computational methods

Molecular geometries for the electronic ground state (S_0) and the triplet state of the model oligomers (n = 1–8) were optimized in the gas phase using density functional theory (DFT) with Becke's three-parameter functional B3LYP[9] and 6-31G** basis set. Hexadecyl ($–C_{16}H_{25}$) side chains were truncated with methyl ($–CH_3$) groups. Broken-symmetry (BS) singlet state calculations were started with a restricted wave-function. $NICS_{iso}(1)$ was computed by the gauge-independent atomic orbital (GIAO) method on the BS optimized geometry by single point energy calculation at the UB3LYP/6-31G** level of theory at 1 Å perpendicularly above the ring plane to account for only the π-electrons' contribution. At this distance, the contribution of the π-electrons is maximized.[10] The diradical index (y) was calculated at UB3LYP/6-31G** level of theory using both HONO and LUNO occupation number and Yamaguchi's formula (Table S1).[11] The spin locations were predicted from natural spin densities of Kohn-Sham molecular orbitals (MO).

4. Supplemental figures S1–S29

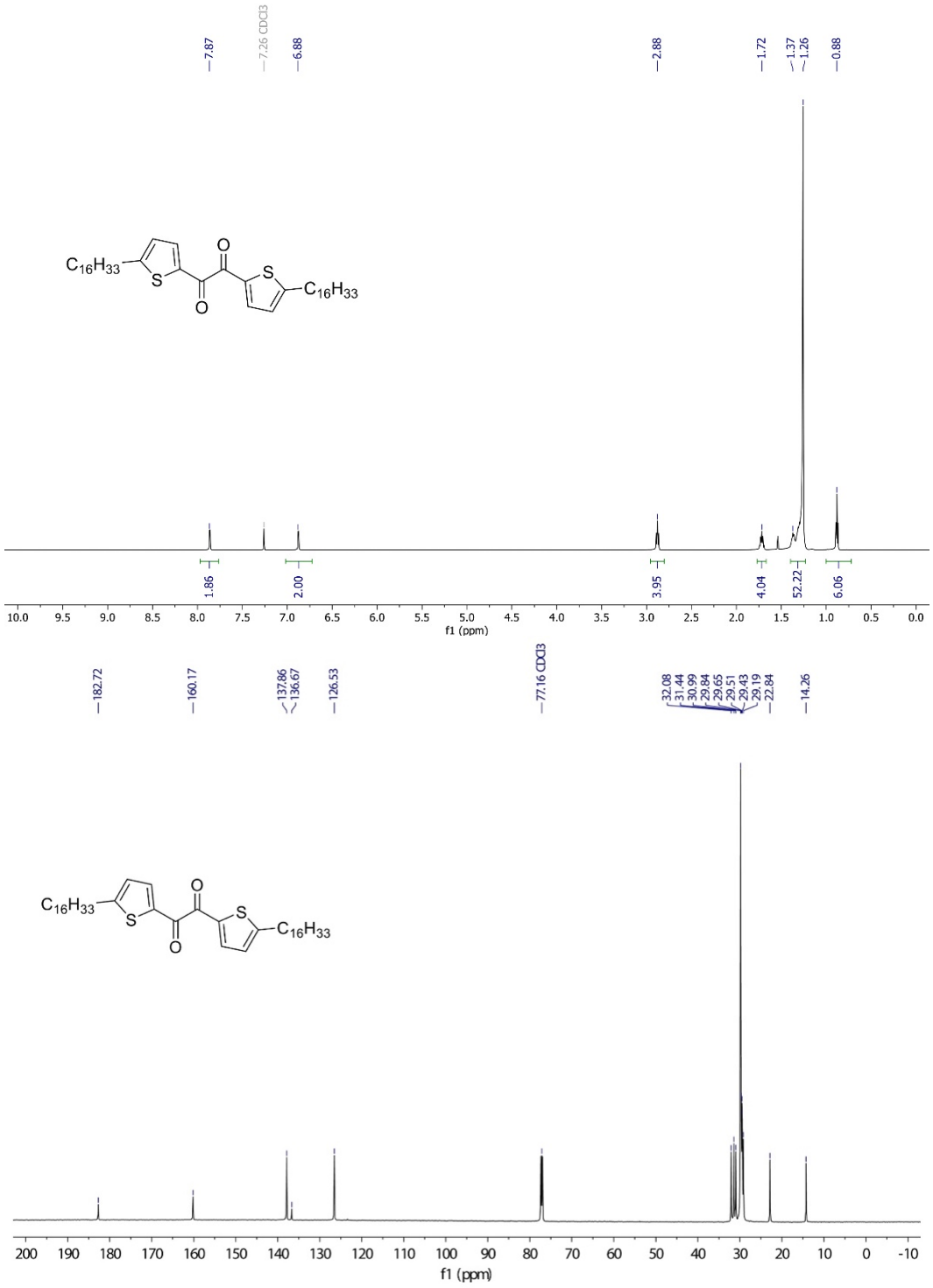

Figure S1. ^{1}H and ^{13}C NMR spectra of compound 1. (Top) ^{1}H NMR spectrum (600 MHz, chloroform-*d*) of 1,2-bis(5-hexadecylthiophen-2-yl)ethane-1,2-dione. (Bottom) ^{13}C NMR spectrum (151MHz, chloroform-*d*) of 1,2-bis(5-hexadecylthiophen-2-yl)ethane-1,2-dione.

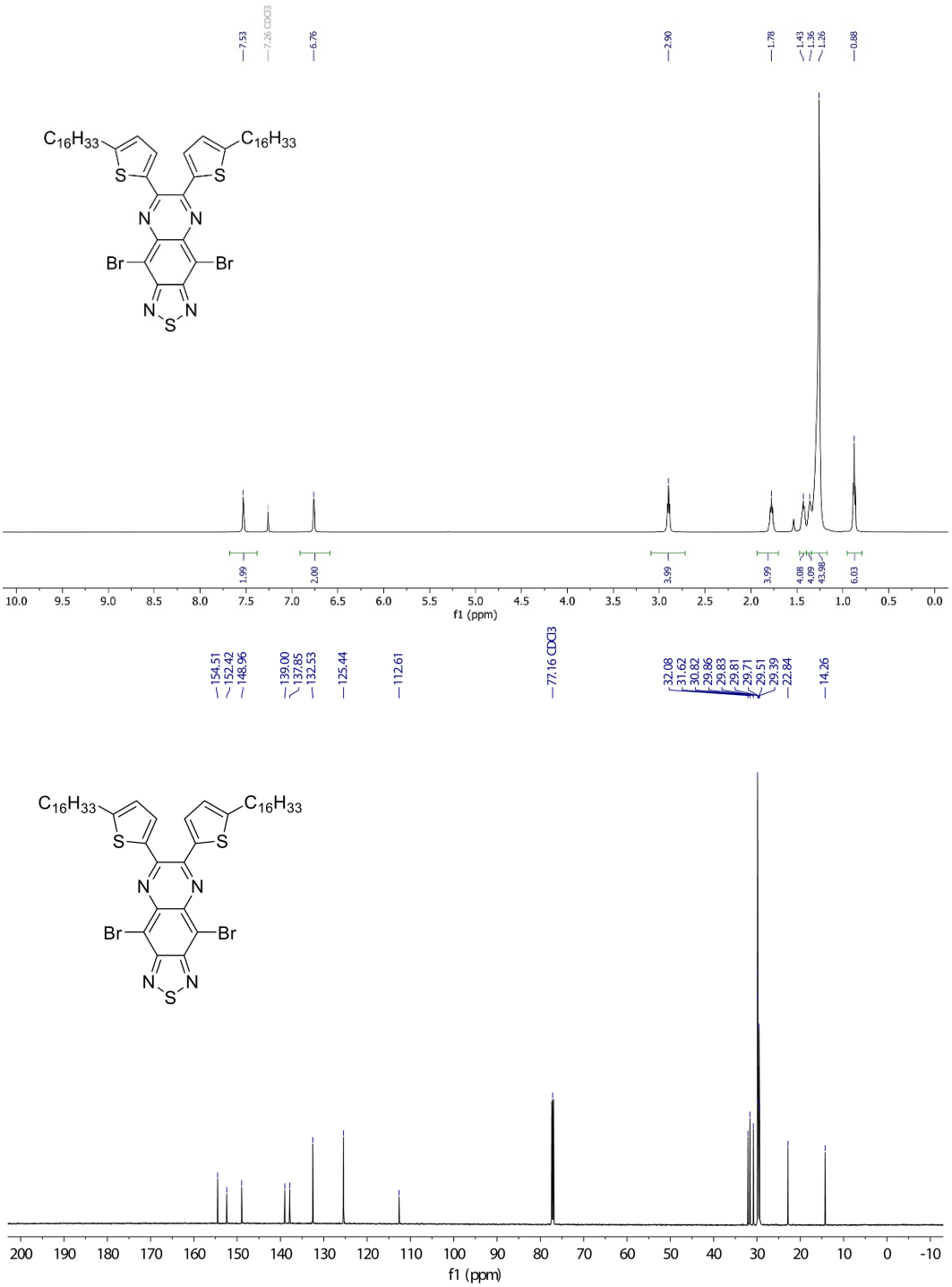

Figure S2. ^{1}H and ^{13}C NMR spectra of compound M2. (Top) ^{1}H NMR spectrum (600 MHz, chloroform-*d*) of 4,9-dibromo-6,7-bis(5-hexadecylthiophen-2-yl)-[1,2,5]thiadiazolo[3,4-*g*]quinoxaline. (Bottom) ^{13}C NMR spectrum (151MHz, chloroform-*d*) of 4,9-dibromo-6,7-bis(5-hexadecylthiophen-2-yl)-[1,2,5]thiadiazolo[3,4-*g*]quinoxaline.

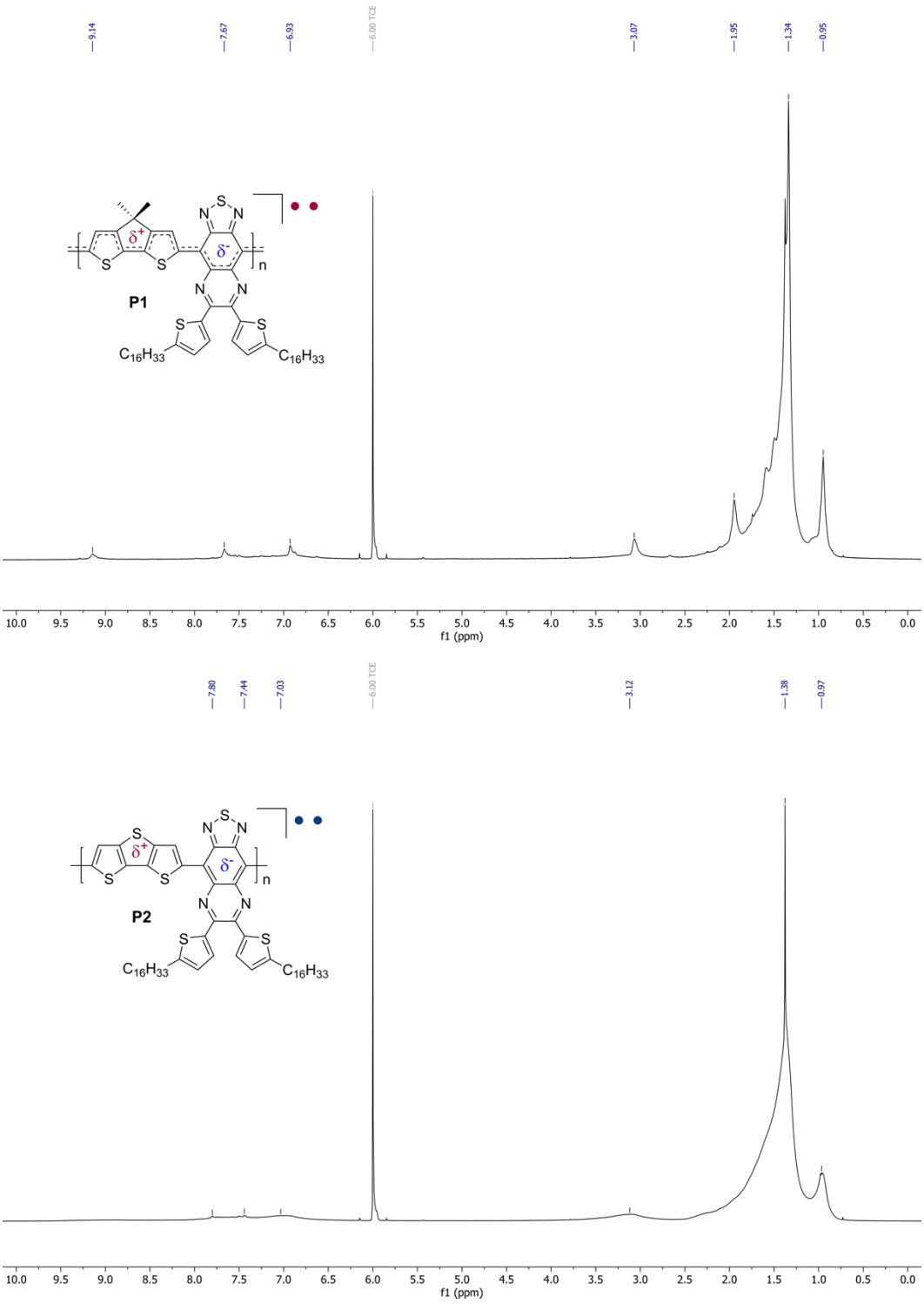

Figure S3. ^{1}H NMR spectra (600 MHz, Tetrachloroethane-d_2, 413 K). (Top) **P1,** (bottom) **P2.**

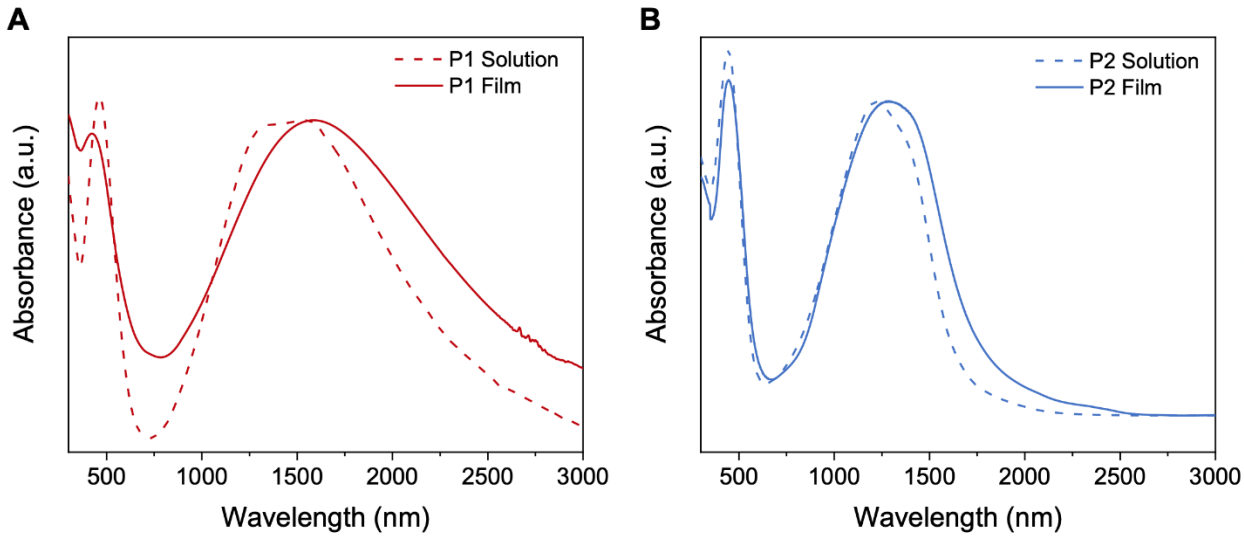

Figure S4. UV–vis–NIR absorption spectra of **P1** (A) and **P2** (B) comparing both the solid-state film absorption and the dilute solution in ClBz indicating strong aggregation behavior.

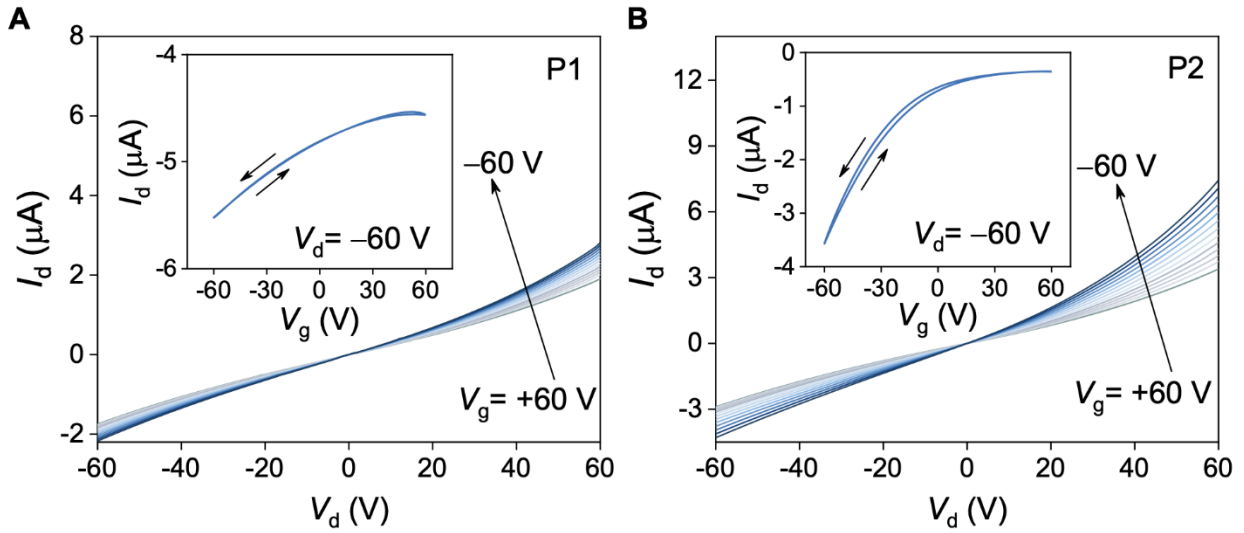

Figure S5. OFET output and transfer (inset) characteristics for **P1** (A) and **P2** (B). In both samples, the output curves do not illustrate distinct linear and saturation regions at varying gate voltages, and the transfer curves do not demonstrate any off-state, indicating the abundant intrinsic charge carriers shielding the field effect.

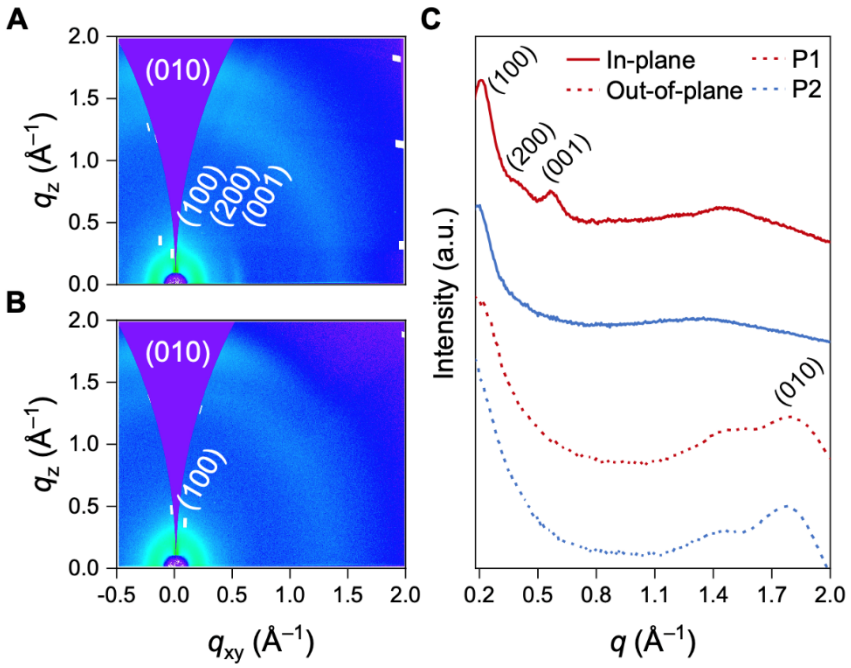

Figure S6. Two-dimensional GIWAXS profiles of **P1** (A) and **P2** (B) (as-cast). (C) One-dimensional line cuts of the integrated in-plane and out-of-plane GIWAXS profiles illustrating distinct backbone packing in P1, π–π stacking, and weakly ordered lamellar stacking for both **P1** and **P2**.

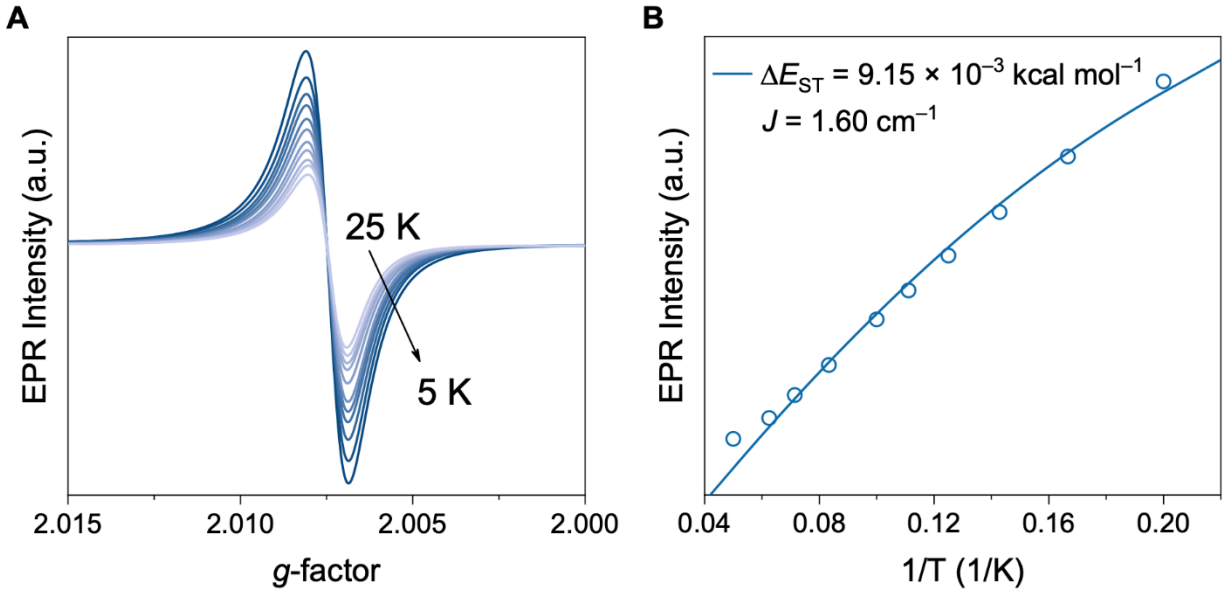

Figure S7. (A) EPR spectra of **P1** solid-state sample from 25 to 5 K and (B) temperature-dependent fit to the Bleaney-Bowers equation with ΔE_{ST} of 9.15 ×10^{-3} kcal mol^{-1}, which demonstrates a slightly larger ΔE_{ST} for the high-spin sample compared to **P1** in solution.

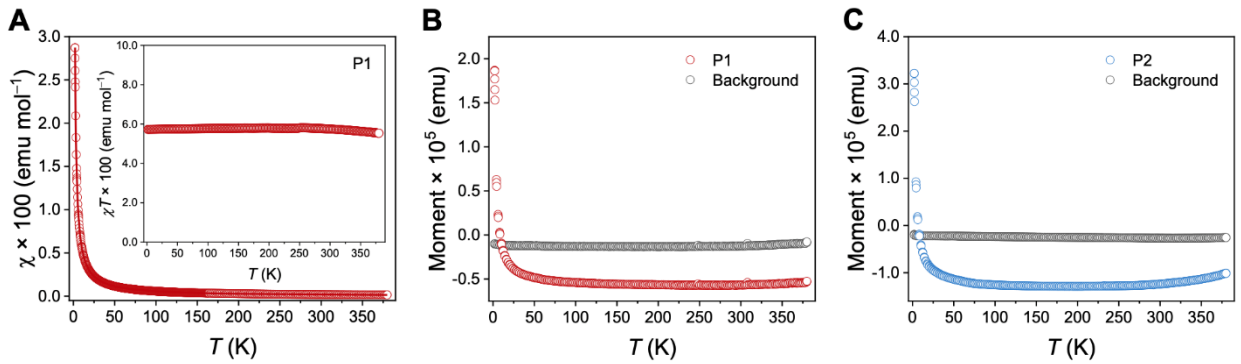

Figure S8. (A) SQUID magnetometry of solid sample. Main plot: Magnetic susceptibility, χ versus T, from 2 to 375 K fit to the Curie-Weiss law (red line). Inset: Observed χT versus T dependence. The unprocessed signal from (B) **P1** and (C) **P2** accompanying background scan used to subtract the diamagnetism due to the sample holder assembly.

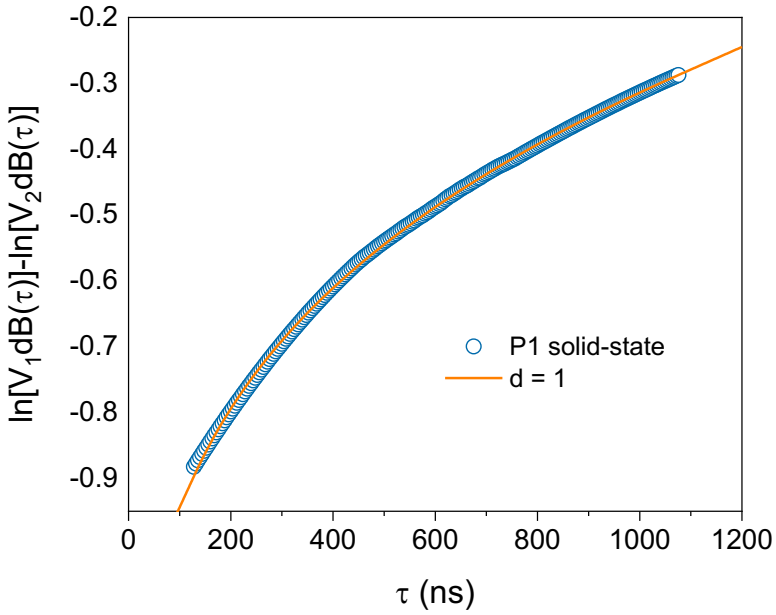

Figure S9. The fractal dimensionality (d) for spatial distribution of electron spins of **P1** was determined from the two-pulse spin echo measurements of instantaneous diffusion. The d = 1 (0.75) for the electron spin distribution at 5 K of solid-state sample demonstrates a one-dimensional intra-chain spin distribution.

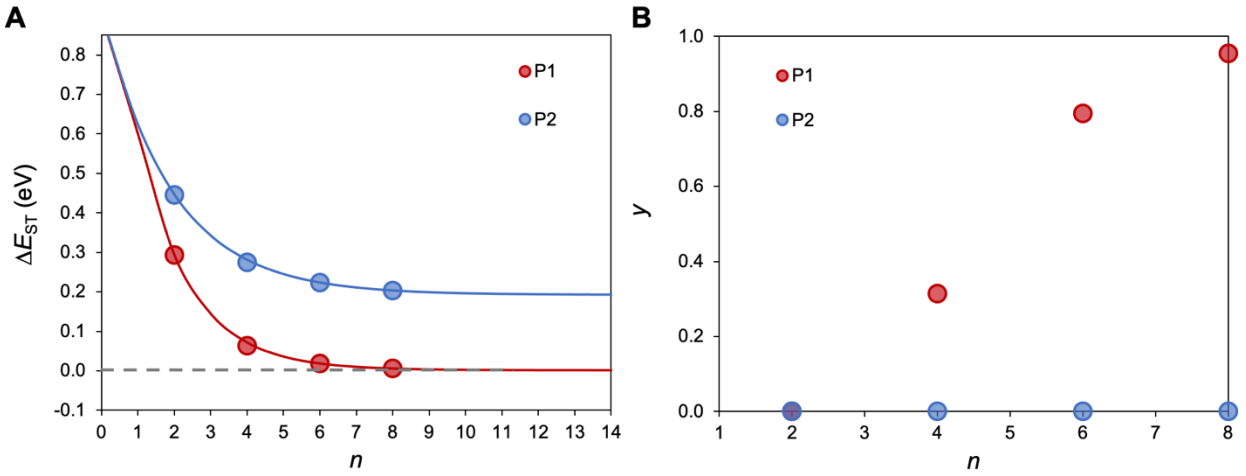

Figure S10. Calculated data for the oligomers (n = 2 – 8) at the UB3LYP/6-31G** level of theory for **P1** and **P2**. (A) ΔE_{ST} of the oligomers and extrapolation of ΔE_{ST} DFT vs. n to the polymer limit ($n \rightarrow \infty$) which gives a horizontal asymptote of 0.0 and 0.2 eV for **P1** and **P2**, respectively which is consistent with experimental results in Figure 5C, F. (B) y vs. n of the oligomers. As n increases, y increases rapidly and trends towards a value of 1.0 for n = 8 in **P1**, while **P2** is essentially closed-shell for $n \leq 6$.

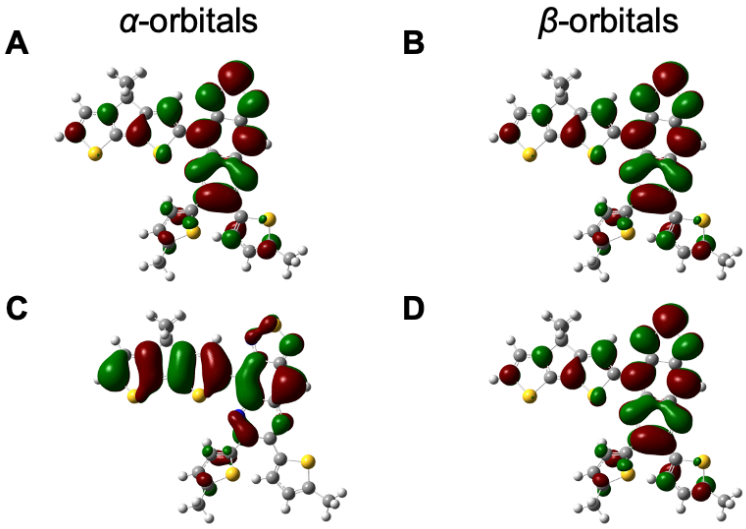

Figure S11. Optimized ground state geometric structures for the single repeat unit (n = 1) of **P1** and pictorial representations of the frontier MOs. (A) α-SUMO and (B) β-SUMO, (C) α-SOMO and (D) β-SOMO of the singlet. The green and red surfaces represent positive and negative signs of the MO at isovalue = 0.02 au, respectively. Color codes for the atoms are: gray for C, blue for N and yellow for S.

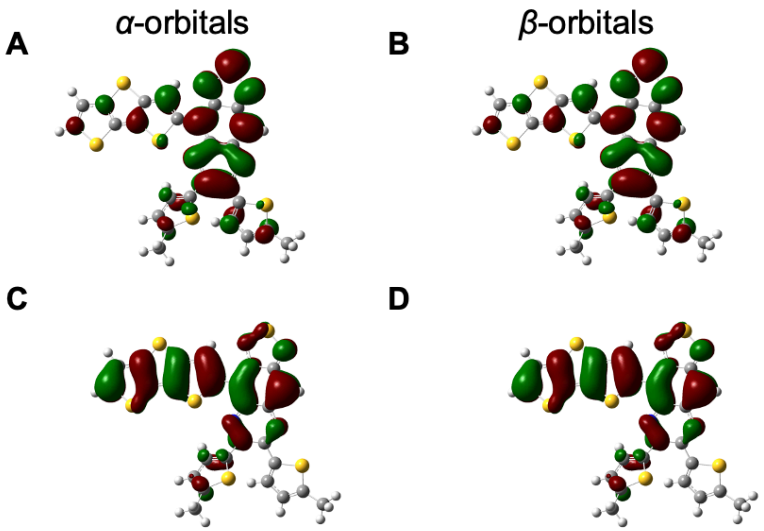

Figure S12. Optimized ground state geometric structures for the single repeat unit (n = 1) of **P2** and pictorial representations of the frontier MOs. (A) α-SUMO and (B) β-SUMO, (C) α-SOMO and (D) β-SOMO of the singlet. The green and red surfaces represent positive and negative signs of the MO at isovalue = 0.02 au, respectively. Color codes for the atoms are: gray for C, blue for N and yellow for S.

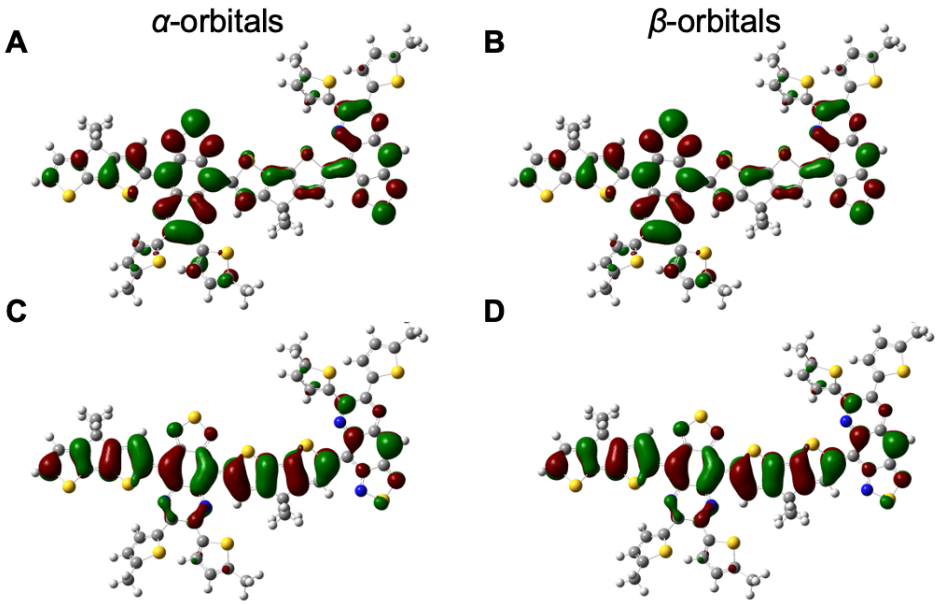

Figure S13. Optimized ground state geometric structures for the dimer (n = 2) of **P1** and pictorial representations of the frontier MOs. (A) α-SUMO and (B) β-SUMO, (C) α-SOMO and (D) β-SOMO of the singlet. The green and red surfaces represent positive and negative signs of the MO at isovalue = 0.02 au, respectively. Color codes for the atoms are: gray for C, blue for N and yellow for S.

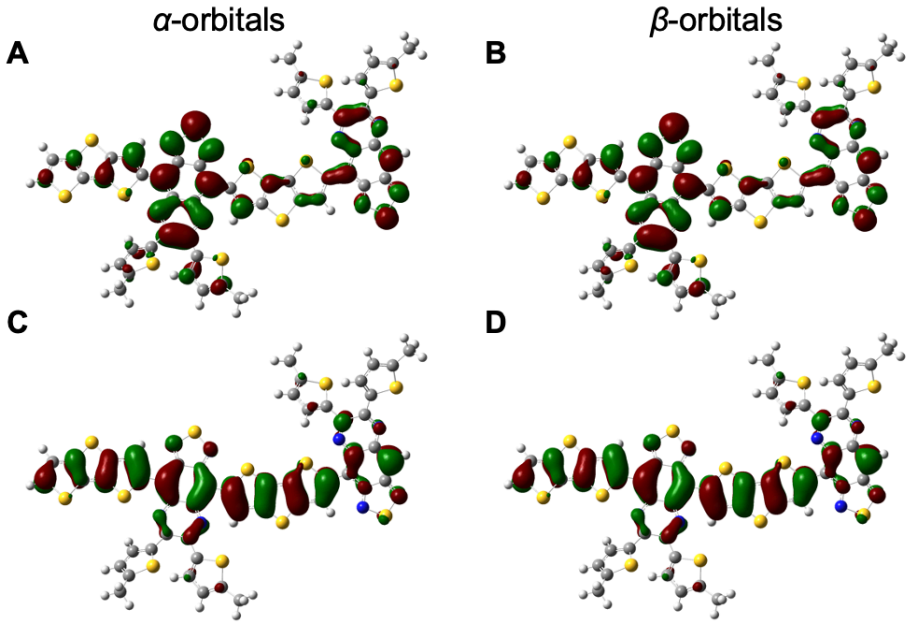

Figure S14. Optimized ground state geometric structures for the dimer (n = 2) of **P2** and pictorial representations of the frontier MOs. (A) α-SUMO and (B) β-SUMO, (C) α-SOMO and (D) β-SOMO of the singlet. The green and red surfaces represent positive and negative signs of the MO at isovalue = 0.02 au, respectively. Color codes for the atoms are: gray for C, blue for N and yellow for S.

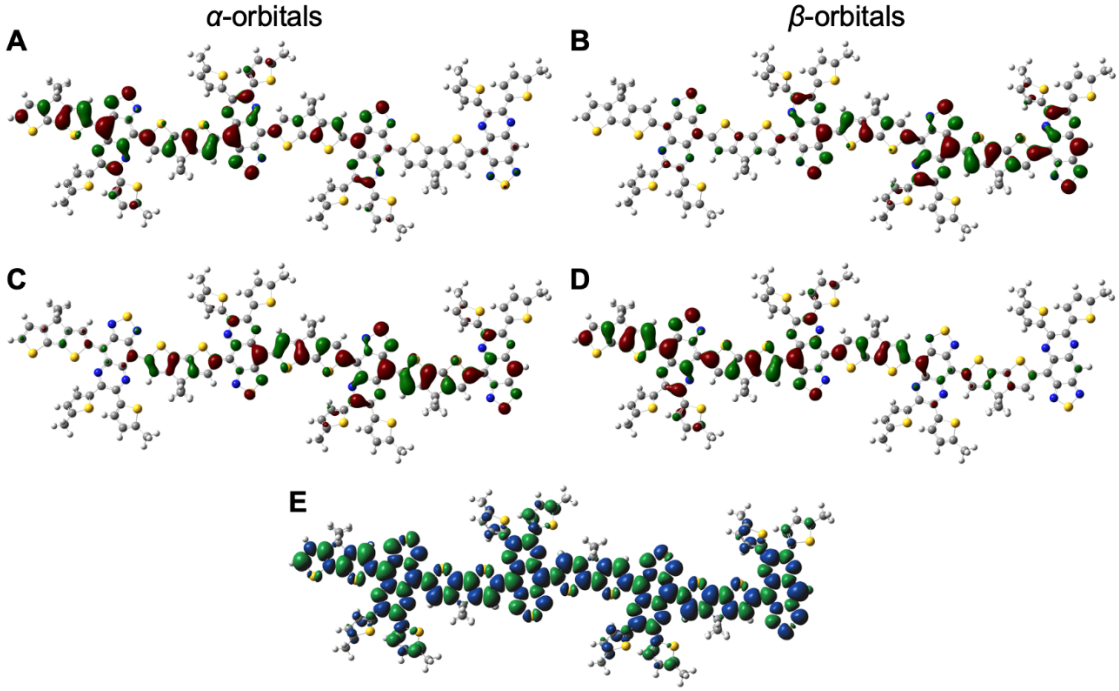

Figure S15. Optimized ground state geometric structures for the tetramer (n = 4) of **P1** and pictorial representations of the frontier MOs and spin density distribution. (A) α-SUMO and (B) β-SUMO, (C) α-SOMO and (D) β-SOMO, and (E) Spin density distribution of the open-shell singlet. The green and red surfaces represent positive and negative signs of the MO at isovalue = 0.02 au, respectively. The blue and green surfaces represent positive and negative contributions of the spin density at an isovalue = 0.0004 au. Color codes for the atoms are: gray for C, blue for N and yellow for S.

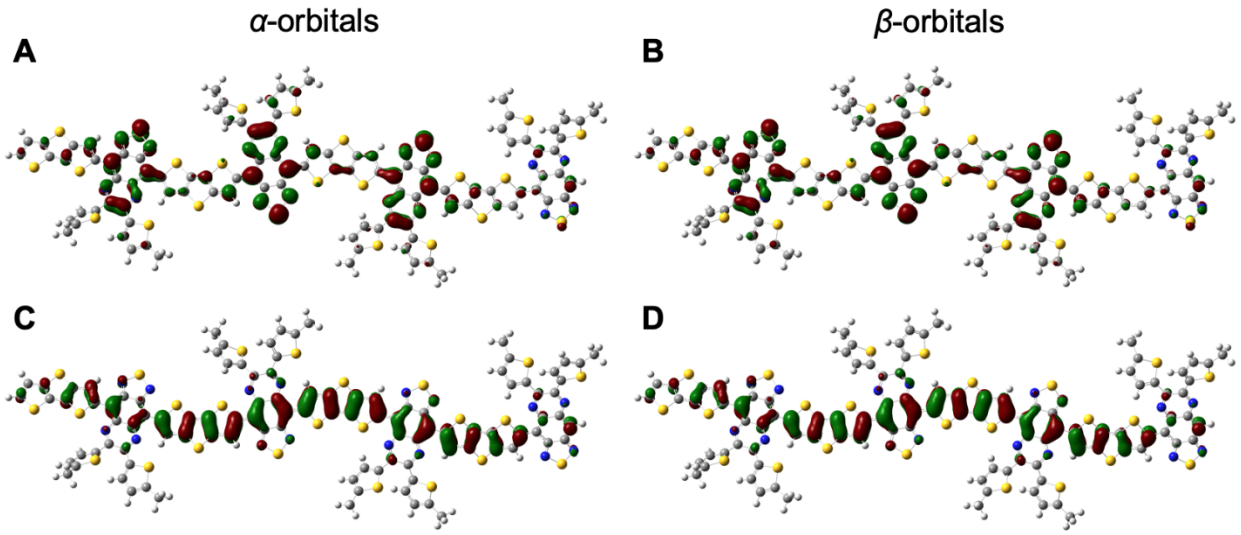

Figure S16. Optimized ground state geometric structures for the tetramer (n = 4) of **P2** and pictorial representations of the frontier MOs. (A) α-SUMO and (B) β-SUMO, (C) α-SOMO and (D) β-SOMO of the singlet. The green and red surfaces represent positive and negative signs of the MO at isovalue = 0.02 au, respectively. Color codes for the atoms are: gray for C, blue for N and yellow for S.

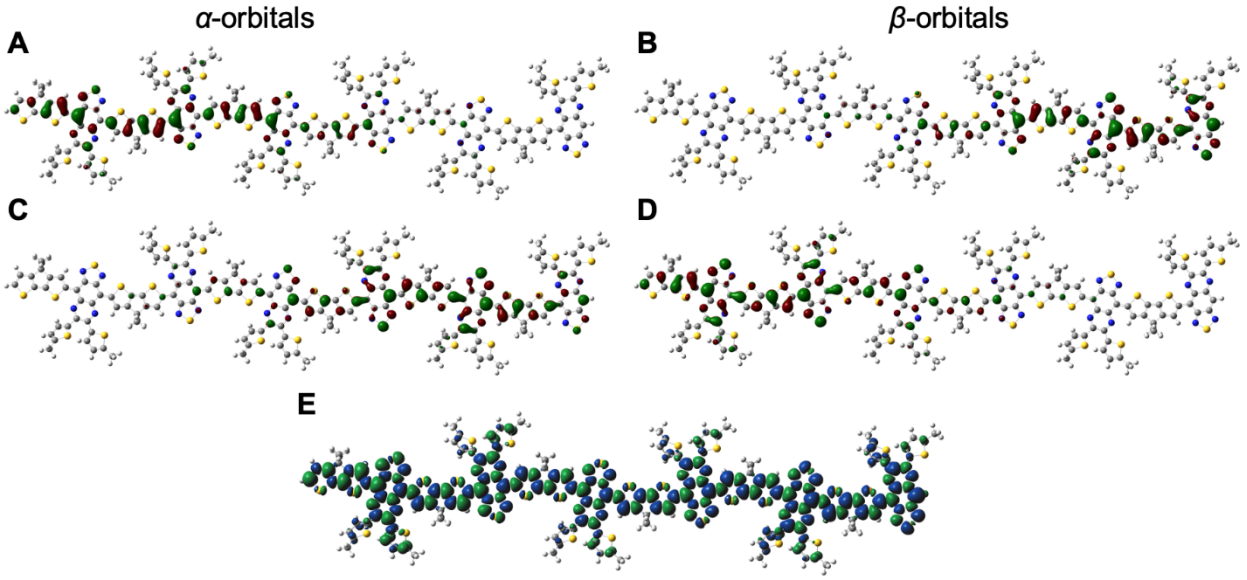

Figure S17. Optimized geometric structures for the hexamer (n = 6) of **P1** and pictorial representations of the frontier MOs and spin density distribution. (A) α-SUMO and (B) β-SUMO, (C) α-SOMO and (D) β-SOMO, and (E) Spin density distribution of the open-shell singlet. The green and red surfaces represent positive and negative signs of the MO at isovalue = 0.02 au, respectively. The blue and green surfaces represent positive and negative contributions of the spin density at an isovalue = 0.0004 au. Color codes for the atoms are: gray for C, blue for N and yellow for S.

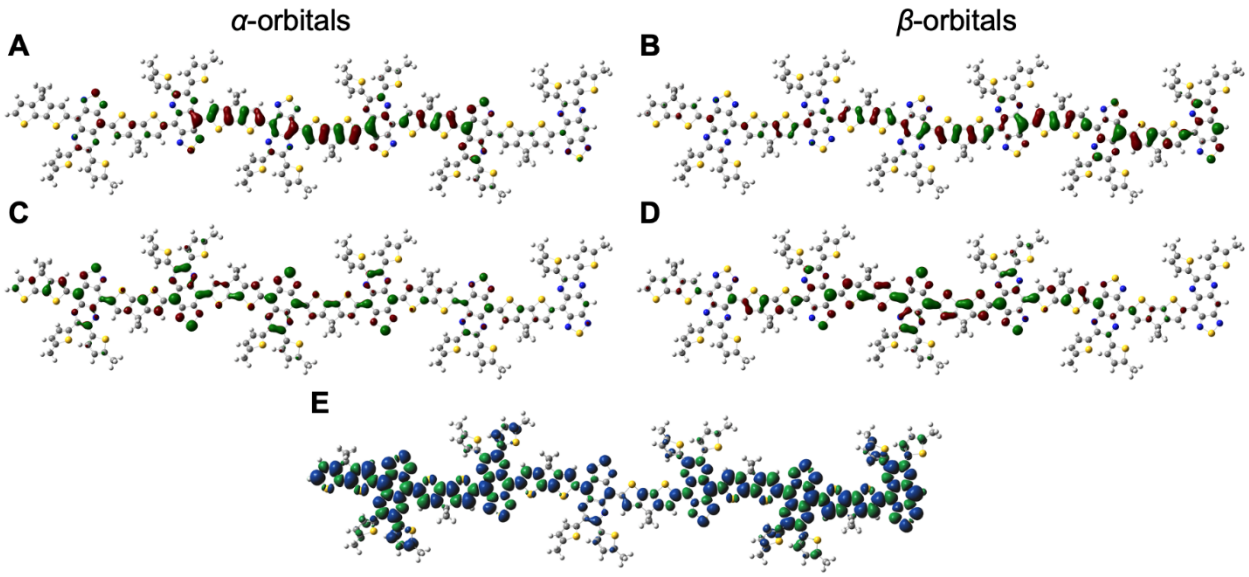

Figure S18. Optimized ground state geometric structures for the hexamer (*n* = 6) of **P1** and pictorial representations of the frontier MOs and spin density distribution. (A) *α*-SUMO and (B) *β*-SUMO, (C) *α*-SOMO and (D) *β*-SOMO, and (E) Spin density distribution of the triplet state. The green and red surfaces represent positive and negative signs of the MO at isovalue = 0.02 au, respectively. The blue and green surfaces represent positive and negative contributions of the spin density at an isovalue = 0.0004 au. Color codes for the atoms are: gray for C, blue for N and yellow for S.

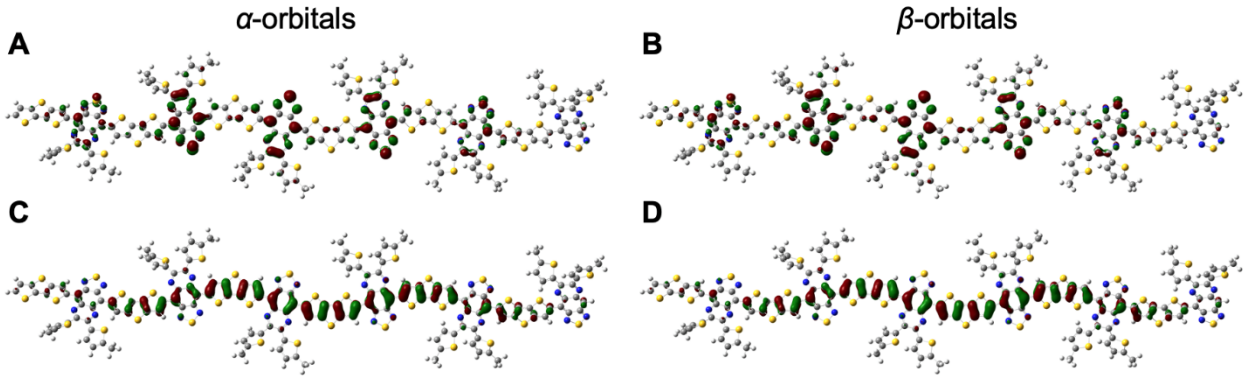

Figure S19. Optimized ground state geometric structures for hexamer (*n* = 6) of **P2** and pictorial representations of the frontier MOs. (A) *α*-SUMO and (B) *β*-SUMO, (C) *α*-SOMO and (D) *β*-SOMO of the singlet. The green and red surfaces represent positive and negative signs of the MO at isovalue = 0.02 au, respectively. Color codes for the atoms are: gray for C, blue for N and yellow for S.

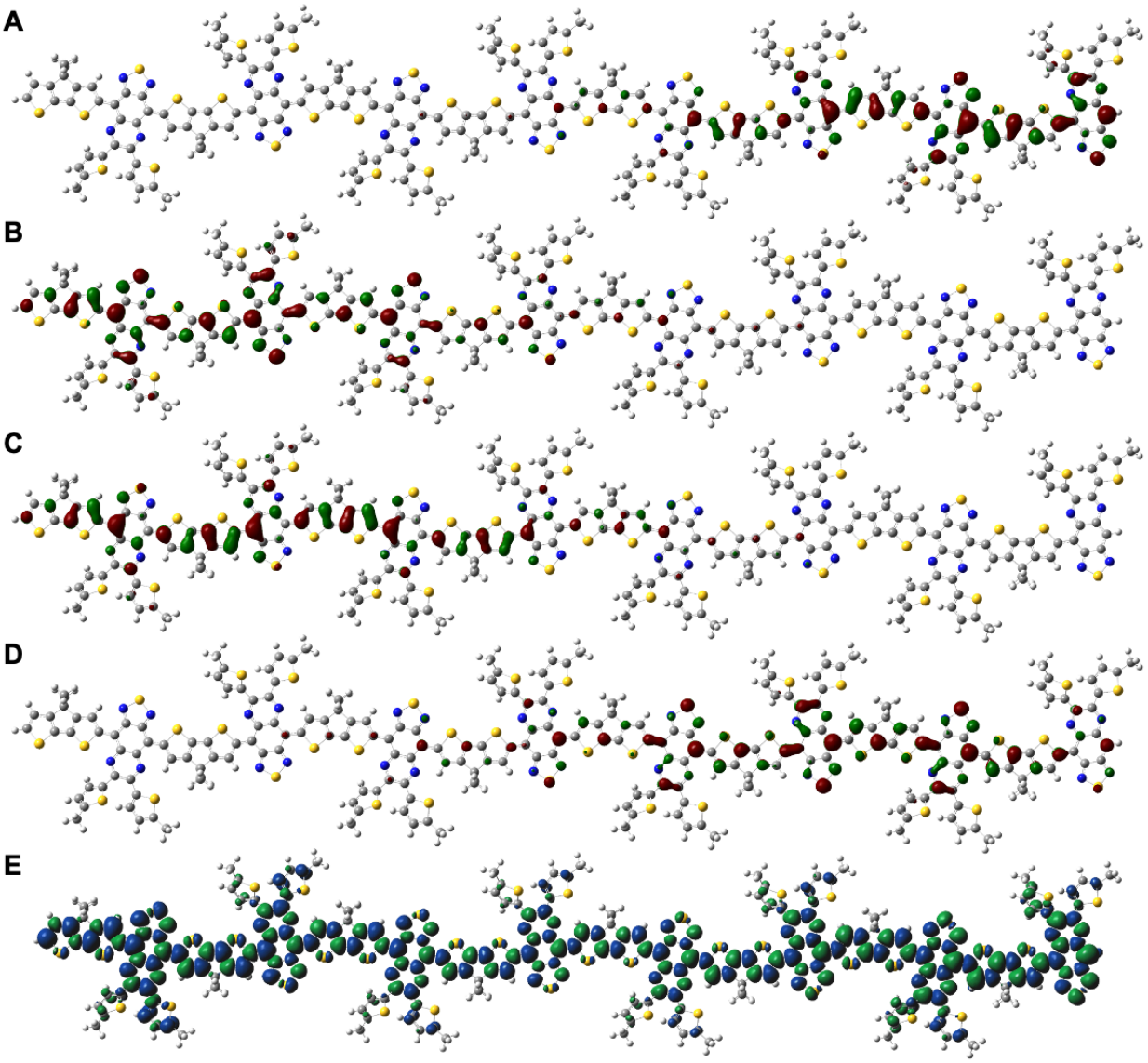

Figure S20. Optimized geometric structures for the octamer (n = 8) of **P1** and pictorial representations of the frontier MOs and spin density distribution. (A) α-SUMO and (C) β-SUMO, (B) α-SOMO and (D) β-SOMO, and (E) Spin density distribution of the open-shell singlet. The green and red surfaces represent positive and negative signs of the MO at isovalue = 0.02 au, respectively. The blue and green surfaces represent positive and negative contributions of the spin density at an isovalue = 0.0004 au. Color codes for the atoms are: gray for C, blue for N and yellow for S.

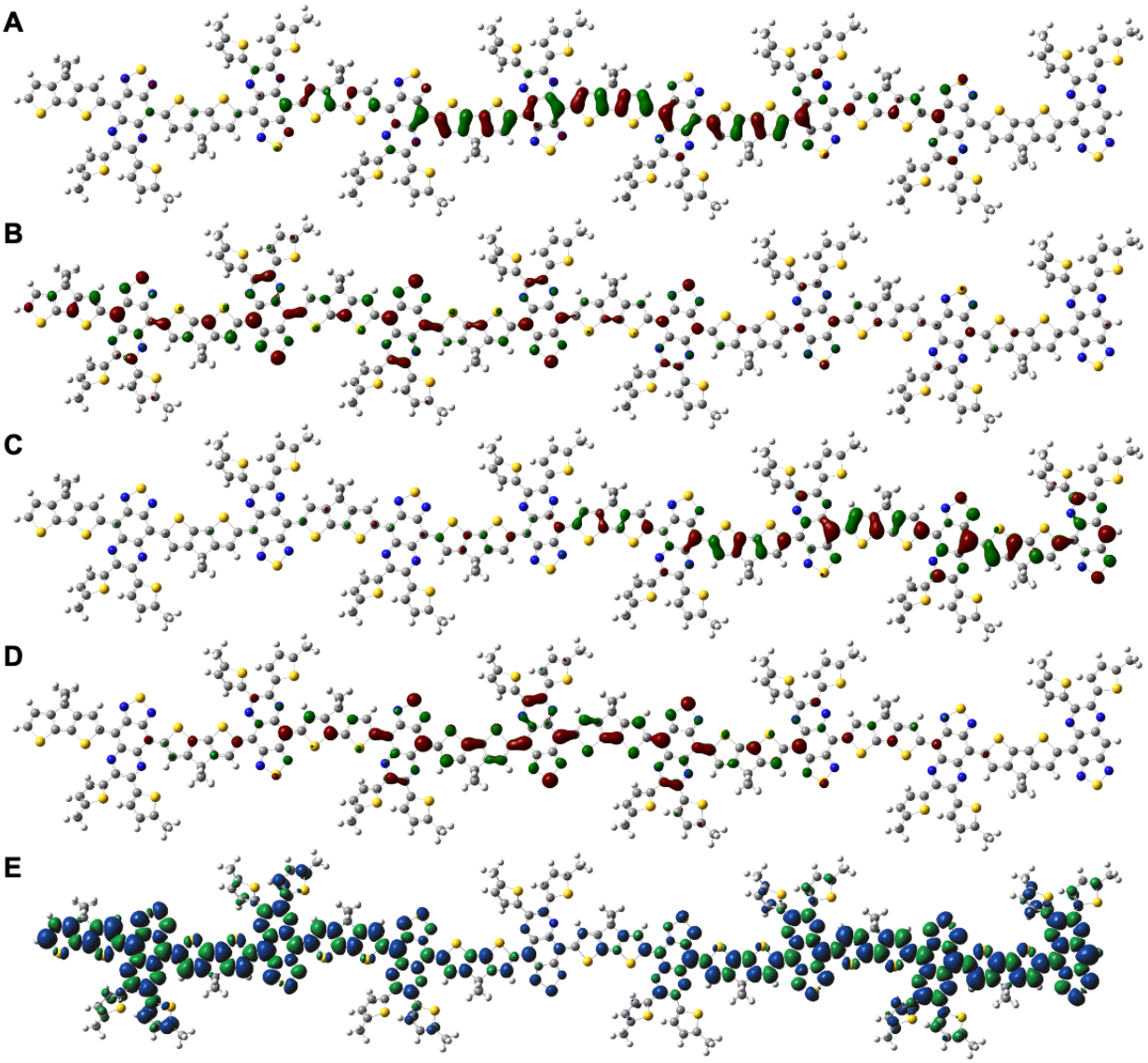

Figure S21. Optimized ground state geometric structures for the octamer (n = 8) of **P1** and pictorial representations of the frontier MOs and spin density distribution. (A) α-SUMO and (C) β-SUMO, (B) α-SOMO and (D) β-SOMO, and (E) Spin density distribution of the triplet state. The green and red surfaces represent positive and negative signs of the MO at isovalue = 0.02 au, respectively. The blue and green surfaces represent positive and negative contributions of the spin density at an isovalue = 0.0004 au. Color codes for the atoms are: gray for C, blue for N and yellow for S.

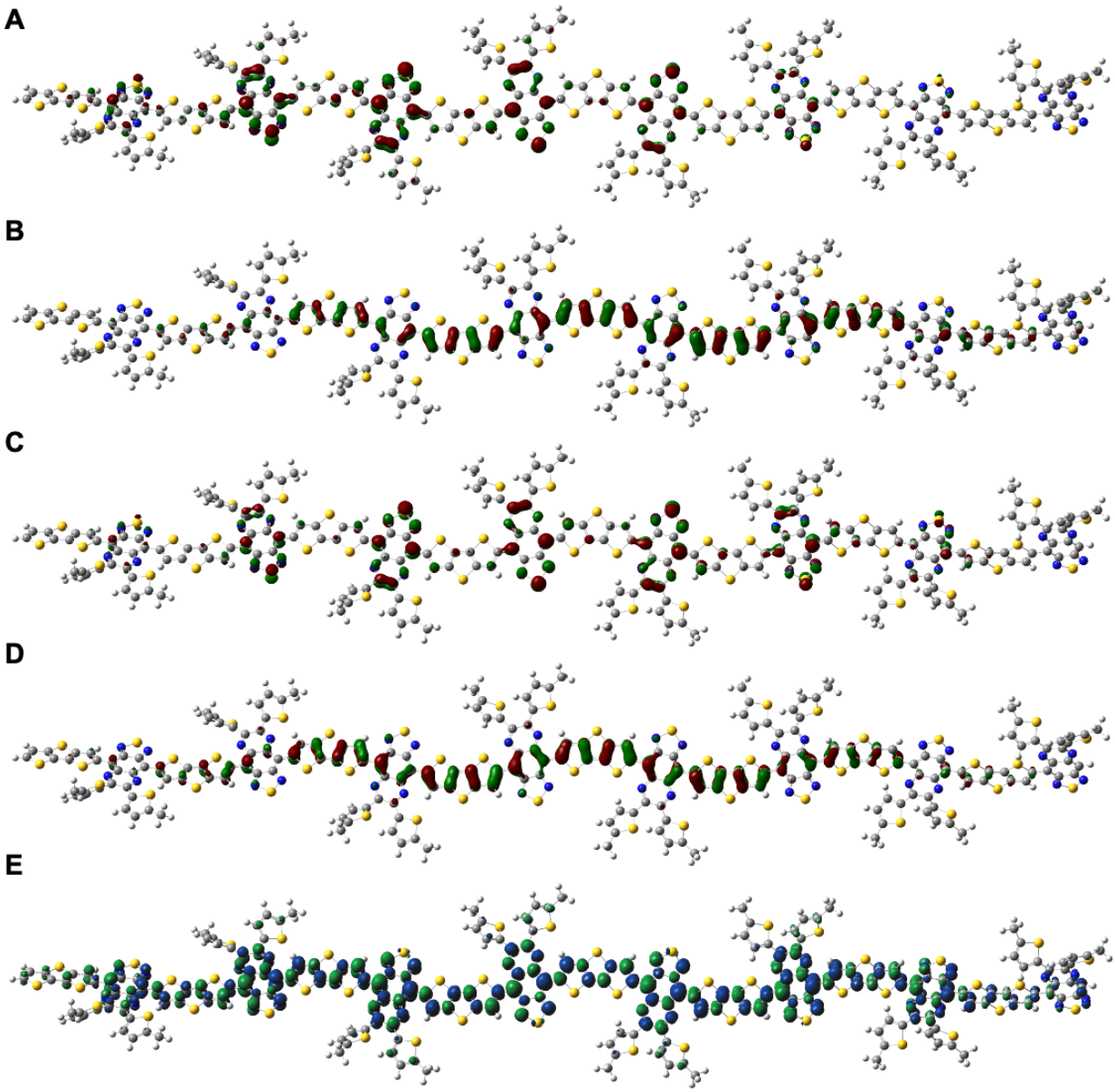

Figure S22. Optimized ground state geometric structures for the octamer (n = 8) of **P2** and pictorial representations of the frontier MOs and spin density distribution. (A) α-SUMO and (C) β-SUMO, (B) α-SOMO and (D) β-SOMO, and (E) Spin density distribution of the open-shell singlet. The green and red surfaces represent positive and negative signs of the MO at isovalue = 0.02 au, respectively. The blue and green surfaces represent positive and negative contributions of the spin density at an isovalue = 0.0004 au. Color codes for the atoms are: gray for C, blue for N and yellow for S.

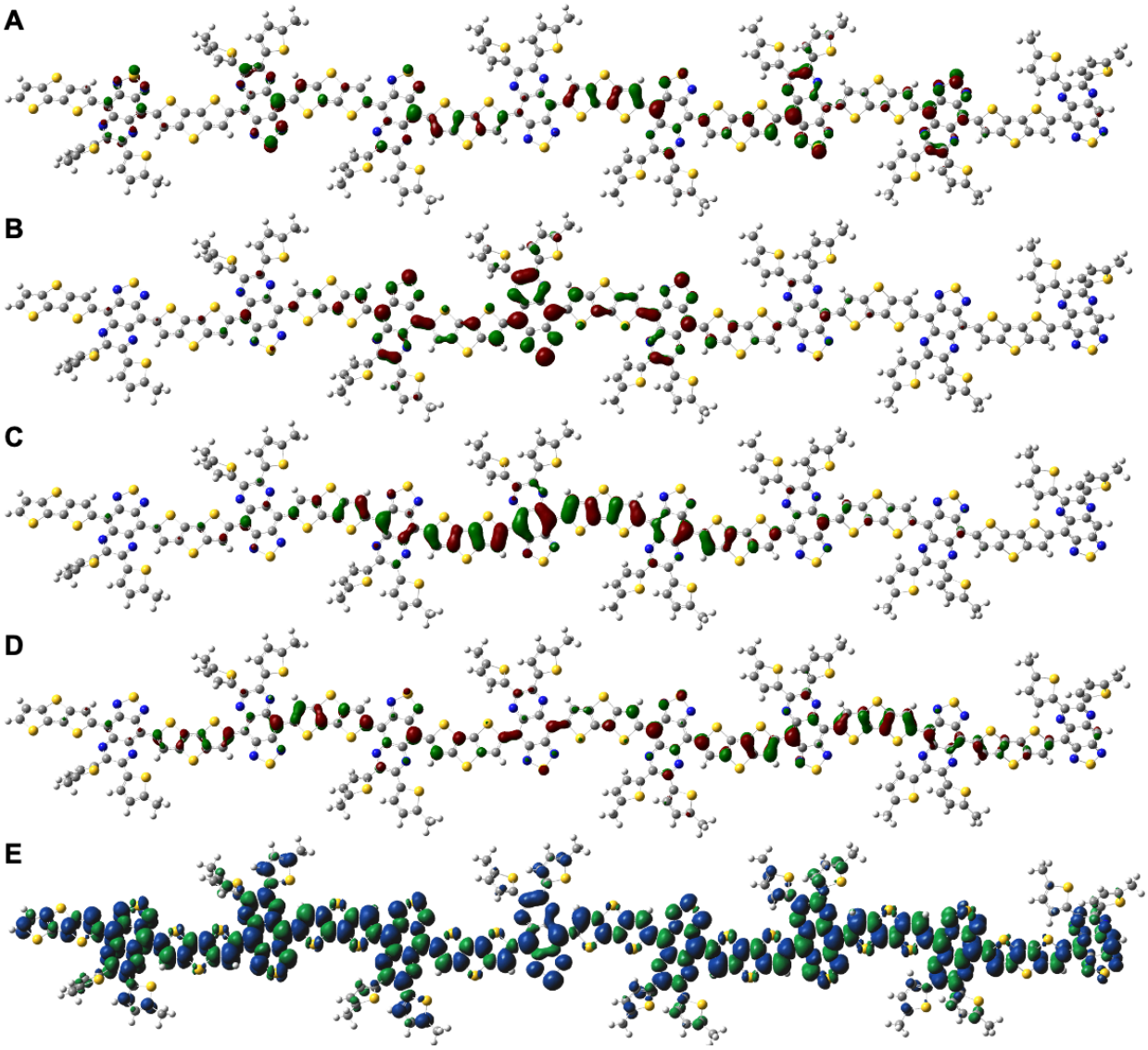

Figure S23. Optimized ground state geometric structures for the octamer (n = 8) of **P2** and pictorial representations of the frontier MOs and spin density distribution. (A) α-SUMO and (C) β-SUMO, (B) α-SOMO and (D) β-SOMO, and (E) Spin density distribution of the triplet state. The green and red surfaces represent positive and negative signs of the MO at isovalue = 0.02 au, respectively. The blue and green surfaces represent positive and negative contributions of the spin density at an isovalue = 0.0004 au. Color codes for the atoms are: gray for C, blue for N and yellow for S.

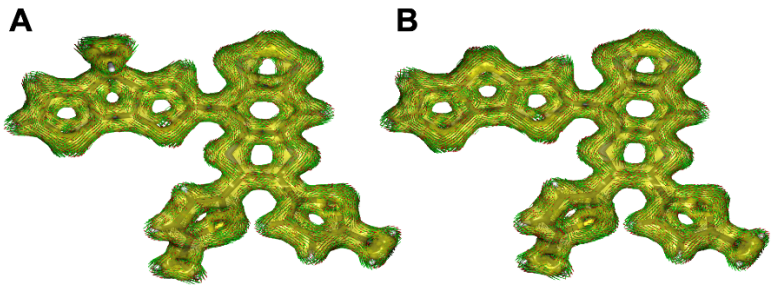

Figure S24. Anisotropy of the induced current density (ACID) of the π-system at CSGT-UB3LYP/6-31G** level of theory for the single repeat unit (*n* = 1) of (A) **P1** singlet and (B) **P2** singlet. The current density vectors plotted on the ACID isosurface indicate ring current (clockwise, counterclockwise) and prevalent delocalization pathways present in these systems.

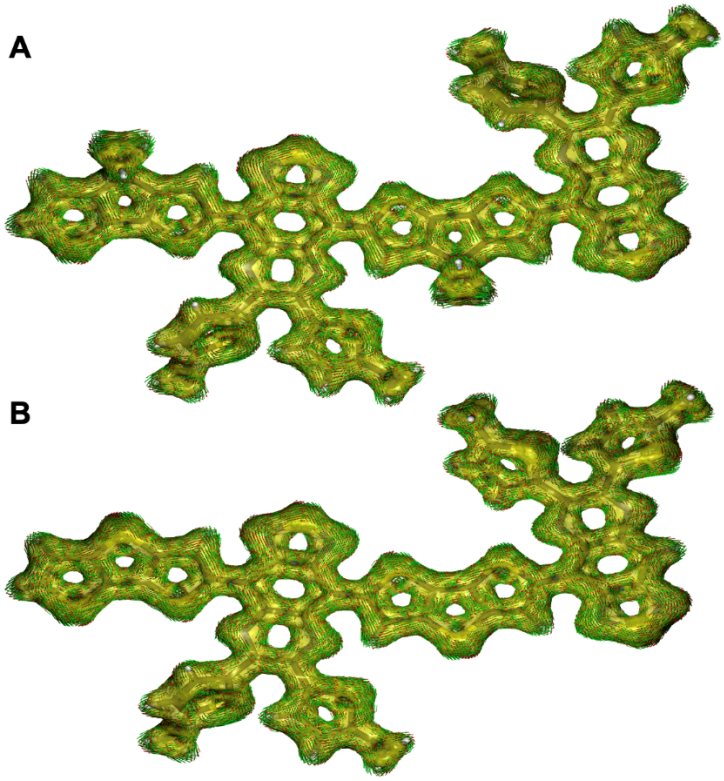

Figure S25. ACID of the π-system at CSGT-UB3LYP/6-31G** level of theory for the dimer (*n* = 2) of (A) **P1** singlet and (B) **P2** singlet. The current density vectors plotted on the ACID isosurface indicate ring current (clockwise, counterclockwise) and prevalent delocalization pathways present in these systems.

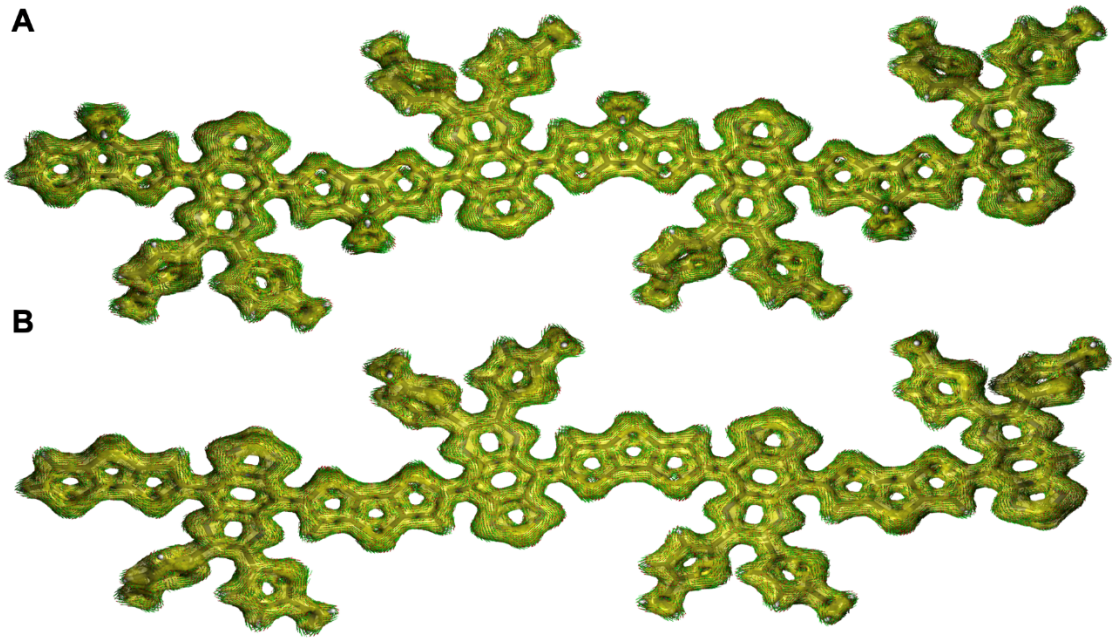

Figure S26. ACID of the π-system at CSGT-UB3LYP/6-31G** level of theory for the tetramer (*n* = 4) of (A) **P1** open-shell singlet and (B) **P2** singlet. The current density vectors plotted on the ACID isosurface indicate ring current (clockwise, counterclockwise) and prevalent delocalization pathways present in these systems.

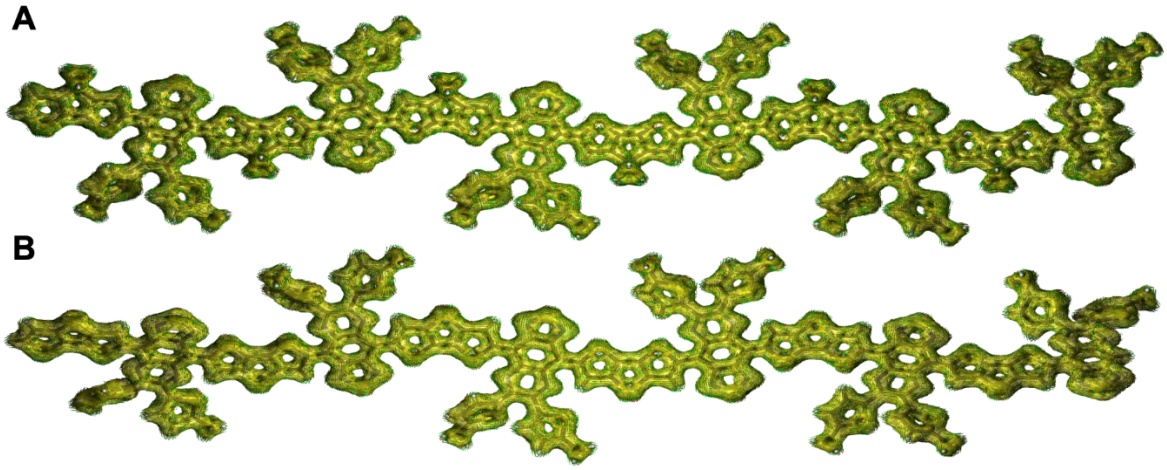

Figure S27. ACID of the π-system at CSGT-UB3LYP/6-31G** level of theory for the hexamer (*n* = 6) of (A) **P1** triplet and (B) **P2** singlet. The current density vectors plotted on the ACID isosurface indicate ring current (clockwise, counterclockwise) and prevalent delocalization pathways present in these systems.

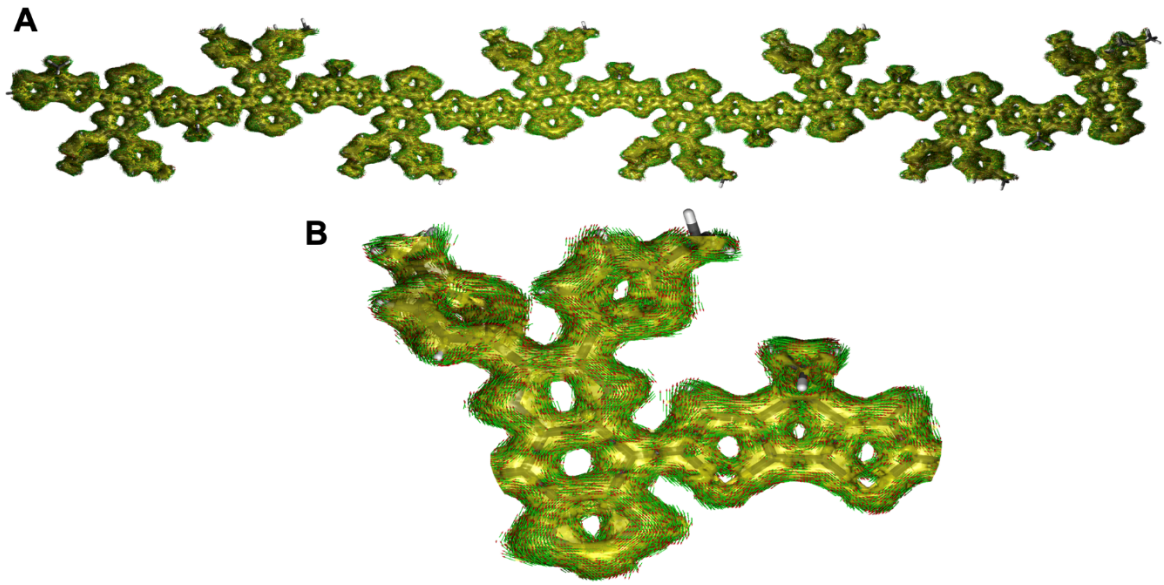

Figure S28. ACID of the π-system at CSGT-UB3LYP/6-31G** level of theory for the octamer (*n* = 8) of the **P1** triplet (A). The blown-up image of the internal repeat unit (B) of the chain shows ring current and delocalization pathways. The current density vectors plotted on the ACID isosurface indicate ring current (clockwise, counterclockwise) and prevalent delocalization pathways present in these systems.

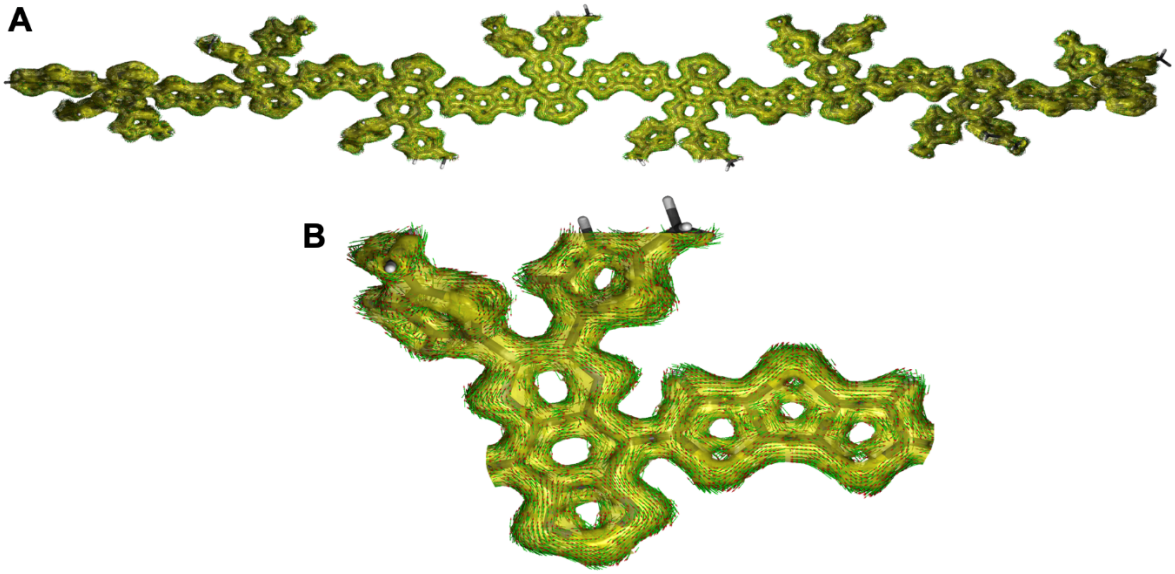

Figure S29. ACID of the π-system at CSGT-UB3LYP/6-31G** level of theory for the octamer (*n* = 8) of the **P2** open-shell singlet (A). The expanded image of the internal repeat unit (B) of the chain shows ring current and delocalization pathways. The current density vectors plotted on the ACID isosurface indicate ring current (clockwise, counterclockwise) and prevalent delocalization pathways present in these systems.

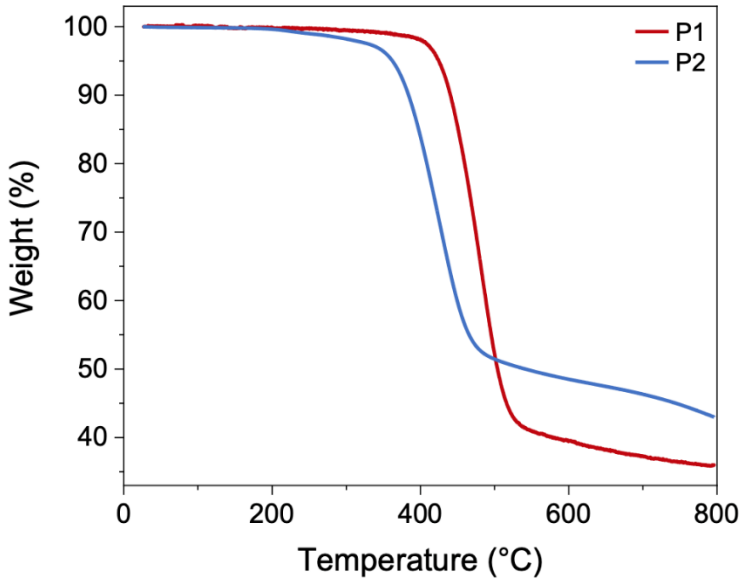

Figure S30. TGA curve of pristine polymer powder showing that the 1% degradation does not occur until approximately 360.2 °C for **P1** and 251.8 °C for **P2** with 5% occurring at approximately 424.7 °C for **P1** and 360.2 °C for **P2**.

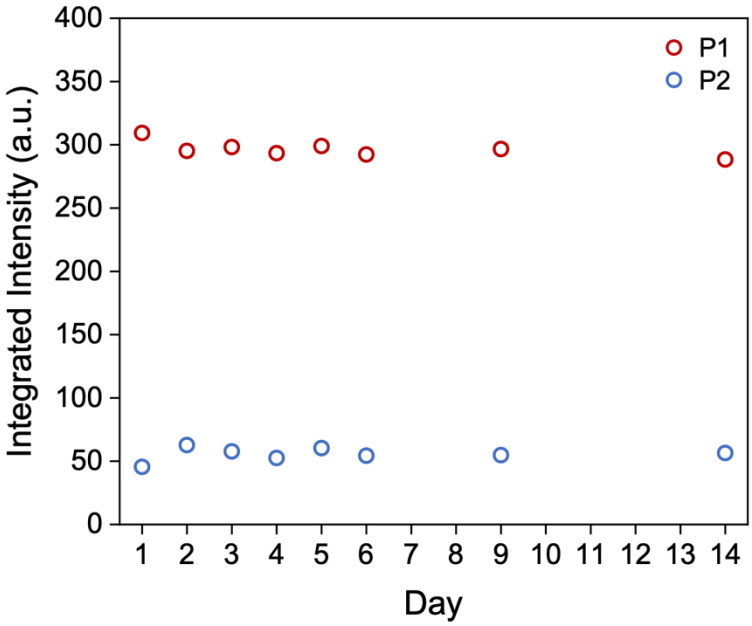

Figure S31. EPR (X-band) spectra of solid samples stored at room temperature under a nitrogen atmosphere showed no discernable changes in spin concentration over a period of 14 days.

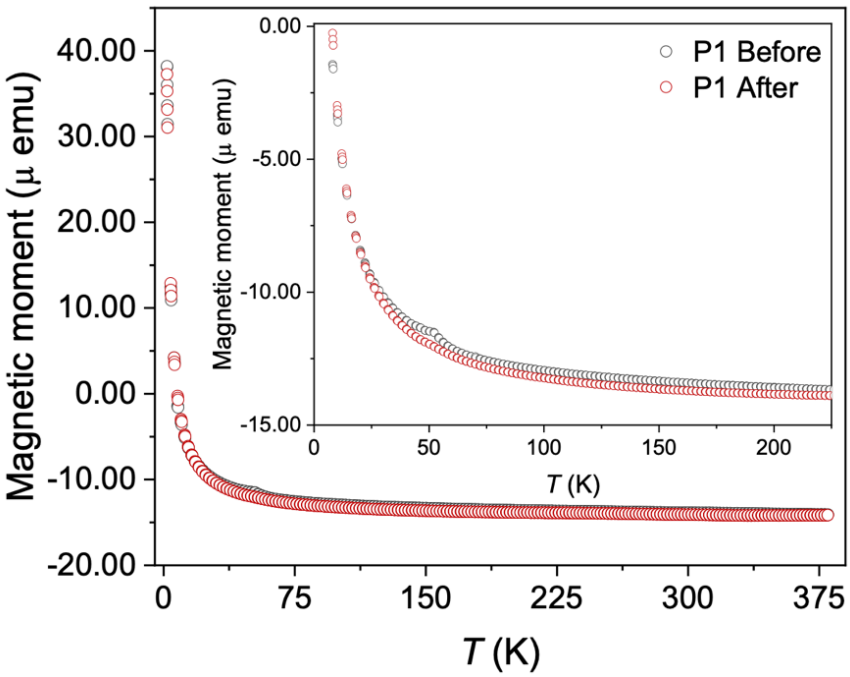

Figure S32. A deviation in the Curie-Weiss behavior can be seen around 50 – 60 K in the magnetic susceptibility plots due to adsorbed oxygen which can occur while preparing the sample for measurement (black circles).

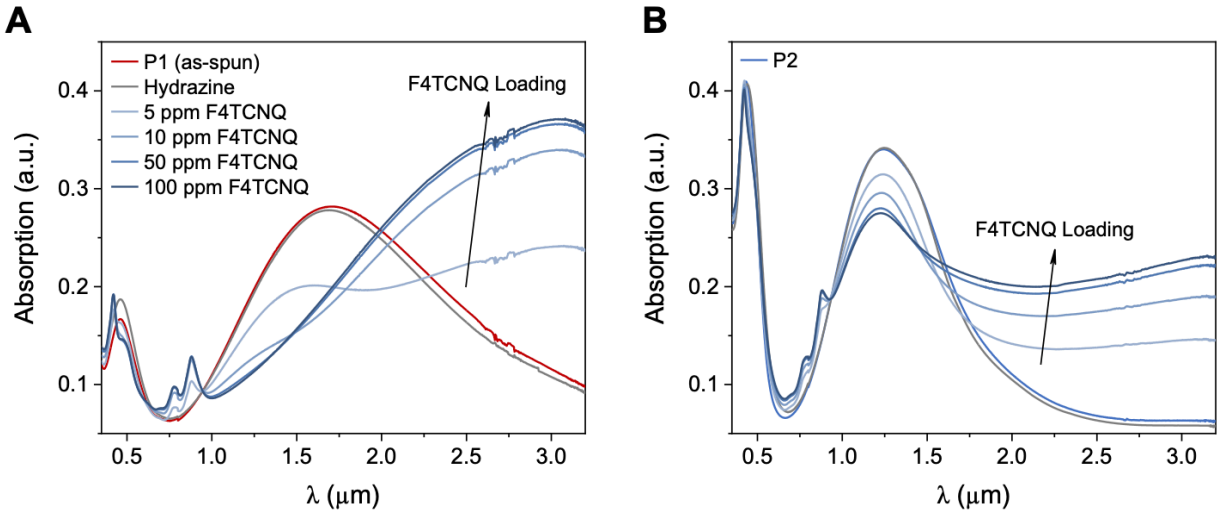

Figure S33. Absorption spectra of **P1**–**P2** (A, B) following sequential doping with varying concentrations of F4TCNQ in acetonitrile. The lack of spectral variance upon addition of hydrazine and the substantial change upon addition of F4TCNQ highlights the undoped nature of **P1**–**P2**.

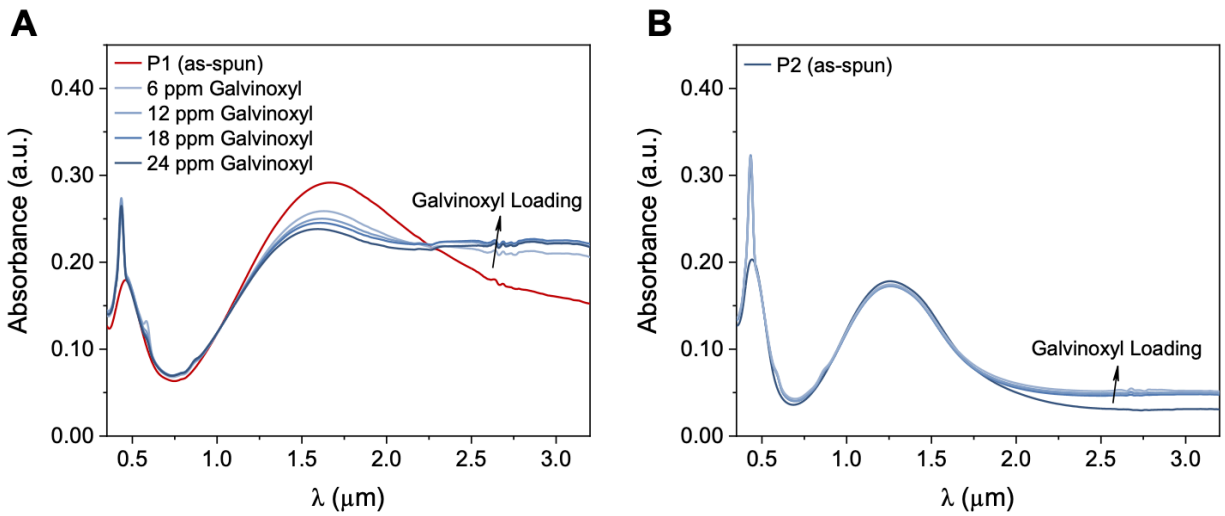

Figure S34. Absorption spectra of **P1**–**P2** (A, B) following sequential doping with varying concentrations of galvinoxyl in acetonitrile.

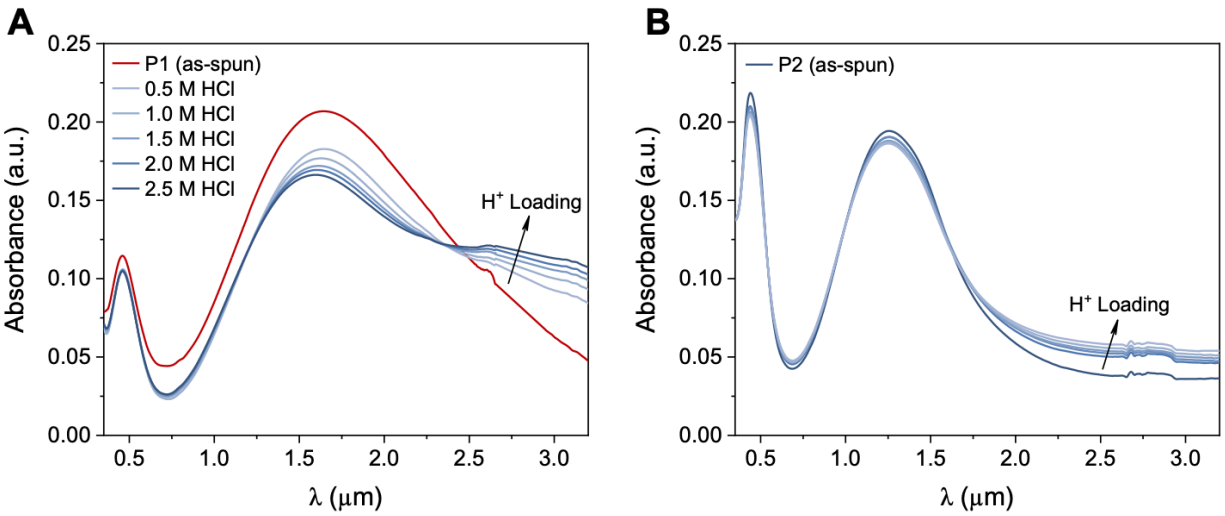

Figure S35. Absorption spectra of **P1**–**P2** (A, B) following sequential doping with varying concentrations of HCl in water.

5. Supplemental tables S1–S11

Table S1. Selected electronic properties of oligomers as a function of number of repeat units.

	n^a	$\Delta E_{ST}{}^b$	nHONO^c	nLUNO^c	$y_0{}^d$
P1	1	–0.740	2.000	0.000	0.000
	2	–0.294	2.000	0.000	0.000
	4	–0.064	1.39742	0.60258	0.314
	6	–0.019	1.10392	0.89608	0.794
	8	–0.006	1.02284	0.95434	0.954
P2	1	–0.838	2.000	0.000	0.000
	2	–0.446	2.000	0.000	0.000
	4	–0.275	2.000	0.000	0.000
	6	–0.224	2.000	0.000	0.000
	8	–0.203	1.97133	0.02867	0.000423

[a]Number of repeat units (n) for the calculated oligomers. [b]Singlet^{BS}-triplet energy gap. [c]Natural orbital occupancies, and [d]diradical character index (y) calculated from Yamaguchi's formula as determined at the UB3LYP/6-31G** level of theory. All energies are in eV, natural orbital occupancies and y are unitless quantities.

Table S2. Tabulated NICS values of the single repeat unit (n = 1)

P1: X = $C(CH_3)_2$
P2: X = S

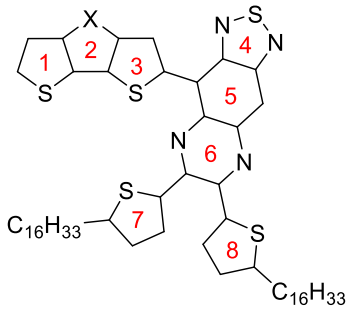

Ring index	P1 Singlet	P2 Singlet
1	–10.17	–9.52
2	–1.94	–8.34
3	–8.09	–7.99
4	–14.65	–15.21
5	–9.51	–9.7
6	–6.8	–6.74
7	–8.27	–9.73
8	–8.62	–8.92

Table S3. Tabulated NICS values of the dimer (*n* = 2)

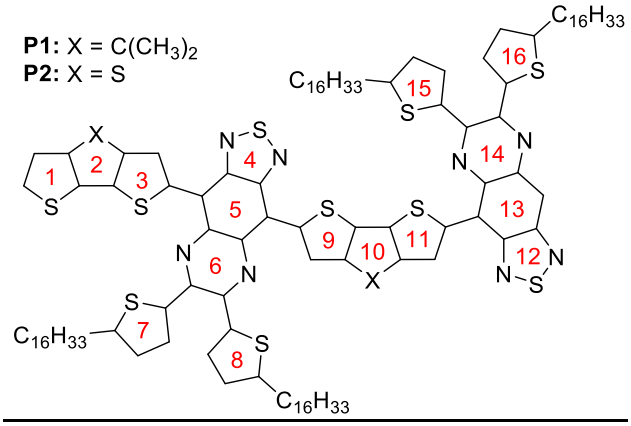

Ring index	P1 Singlet	P2 Singlet
1	–9.29	–8.66
2	–2.28	–7.65
3	–7.61	–6.94
4	–13.48	–13.19
5	–6.47	–7.07
6	–6.36	–6.65
7	–8.37	–10.11
8	–8.98	–8.44
9	–7.05	–6.98
10	–2.22	–6.69
11	–7.09	–6.77
12	–14.38	–14.01
13	–8.15	–8.65
14	–6.36	–6.38
15	–9.41	–8.05
16	–8.93	–8.84

Table S4. Tabulated NICS values of the tetramer (*n* = 4)

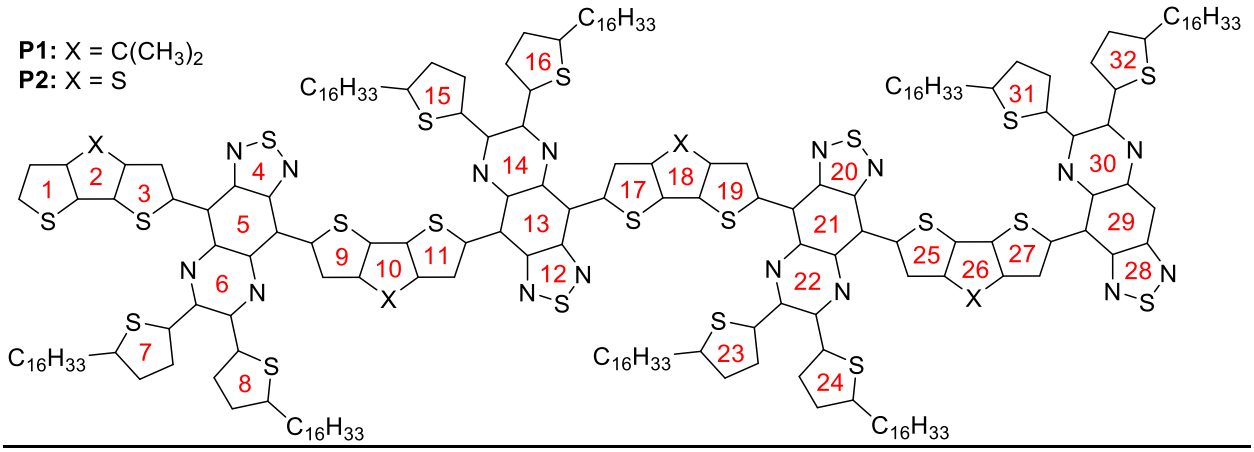

Ring index	P1 Singlet	P2 Singlet	Ring index	P1 Singlet	P2 Singlet
1	–10.11	–8.86	**17**	–7.01	–7.35
2	–1.93	–7.54	**18**	–1.94	–5.96
3	–8.37	–7.5	**19**	–6.8	–6.34
4	–12.69	–13.97	**20**	–12.71	–14.09
5	–5.5	–6.91	**21**	–4.83	–6.64
6	–6.6	–6.62	**22**	–6.78	–6.6
7	–9.15	–9.91	**23**	–8.95	–7.73
8	–8.41	–8.41	**24**	–7.96	–8.49
9	–7.16	–7.3	**25**	–7.7	–7.12
10	–1.9	–6.51	**26**	–1.81	–7.09
11	–7.02	–6.78	**27**	–7.28	–6.26
12	–12.37	–13.68	**28**	–13.46	–14.91
13	–4.44	–6.43	**29**	–7.79	–8.7
14	–6.79	–6.32	**30**	–6.4	–6.4
15	–8.57	–9.19	**31**	–9.36	–9.19
16	–8.62	–8.92	**32**	–8.27	–9.02

Table S5. Tabulated NICS values of the hexamer (*n* = 6)

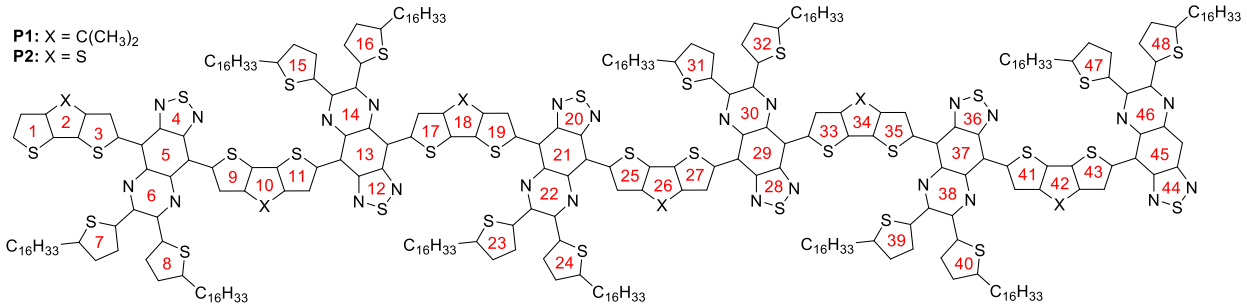

Ring index	P1 Triplet	P2 Singlet	Ring index	P1 Triplet	P2 Singlet	Ring index	P1 Triplet	P2 Singlet
1	–9.38	–9.46	**17**	–5.47	–7.18	**33**	–5.9	–7.79
2	–2.03	–8.46	**18**	–2.04	–6.64	**34**	–2	–6.59
3	–6.89	–8.34	**19**	–5.18	–7.13	**35**	–6.06	–8.11
4	–11.88	–15	**20**	–10.42	–14.14	**36**	–10.76	–14.73
5	–3.52	–6.93	**21**	–1.32	–6.46	**37**	–2.66	–6.56
6	–6.34	–6.59	**22**	–6.58	–6.57	**38**	–6.46	–6.69
7	–9.63	–7.76	**23**	–8.53	–8.19	**39**	–7.96	–9.33
8	–9.13	–8.56	**24**	–8.7	–8.54	**40**	–8.85	–9.4
9	–6.06	–6.7	**25**	–5.28	–7.22	**41**	–5.73	–6.98
10	–2.02	–6.92	**26**	–2.05	–6.78	**42**	–1.99	–5.88
11	–5.73	–6.48	**27**	–5.16	–9	**43**	–6.1	–6.45
12	–10.45	–15.12	**28**	–10.97	–13.63	**44**	–13.85	–16.04
13	–1.89	–6.3	**29**	–1.52	–6.27	**45**	–7.27	–8.38
14	–6.53	–6.32	**30**	–6.58	–6.34	**46**	–6.42	–6.45
15	–9.37	–8.49	**31**	–9.77	–8.76	**47**	–9.15	–9.22
16	–9.12	–9.47	**32**	–8.04	–9.1	**48**	–8.8	–9.5

Table S6. Tabulated NICS values of the octamer (*n* = 8)

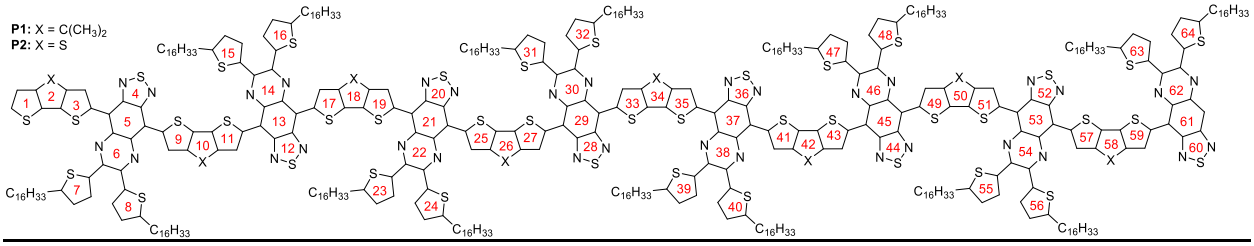

Ring index	P1 Triplet	P2 Singlet	Ring index	P1 Triplet	P2 Singlet	Ring index	P1 Triplet	P2 Singlet	Ring index	P1 Triplet	P2 Singlet
1	–10.99	–9.22	**17**	–5.11	–6.59	**33**	–6.5	–6.8	**49**	–5.67	–7.57
2	–1.94	–7.27	**18**	–2.05	–7.72	**34**	–2.05	–6.09	**50**	–2.03	–6.32
3	–6.77	–6.73	**19**	–4.64	–6.1	**35**	–6.65	–6.67	**51**	–6.6	–7.67
4	–12	–13.37	**20**	–11.55	–13.81	**36**	–11.9	–13.94	**52**	–11.95	–14.02
5	–3.81	–6.92	**21**	–1.66	–6.33	**37**	–1.3	–6.42	**53**	–2.94	–6.59
6	–6.52	–6.65	**22**	–6.45	–6.6	**38**	–6.73	–6.65	**54**	–6.71	–6.61
7	–9.42	–7.99	**23**	–8.33	–8.67	**39**	–8.02	–8.5	**55**	–9.25	–8.16
8	–8.27	–9.79	**24**	–8.06	–9.02	**40**	–9.96	–7.59	**56**	–8.22	–8.99
9	–6.7	–9.04	**25**	–5.27	–6.8	**41**	–7.01	–6.96	**57**	–10.45	–6.53
10	–2.02	–7.1	**26**	–2.02	–6.28	**42**	–2.02	–6.41	**58**	–1.88	–6.47
11	–5.1	–6.48	**27**	–5.31	–6.74	**43**	–6.83	–6.69	**59**	–8.57	–6.55
12	–9.04	–13.84	**28**	–10.65	–12.78	**44**	–11.2	–13.23	**60**	–13.99	–15.51
13	–2.19	–6.32	**29**	–1.45	–6.31	**45**	–1.74	–6.28	**61**	–7.4	–8.42
14	–6.4	–6.39	**30**	–6.71	–6.29	**46**	–6.74	–6.34	**62**	–6.43	–6.33
15	–8.86	–8.16	**31**	–8.34	–8.44	**47**	–9.48	–8.34	**63**	–8.33	–8.79
16	–8.94	–10.53	**32**	–7.84	–8.51	**48**	–9.11	–8.63	**64**	–9.86	–8.78

Table S7. Tabulated bond length values (Å) of the single repeat unit (*n* = 1)

P1: X = $(CH_3)_2$
P2: X = S

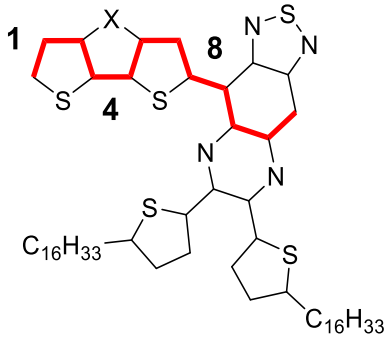

Bond Index	P1 Singlet	P2 Singlet
1	1.3740	1.3681
2	1.4185	1.4227
3	1.3869	1.3959
4	1.4373	1.4178
5	1.3894	1.3949
6	1.4008	1.4069
7	1.3997	1.3913
8	1.4480	1.4527
9	1.4220	1.4188
10	1.4515	1.4516
11	1.3867	1.3864

Table S8. Tabulated bond length values (Å) of the dimer (*n* = 2)

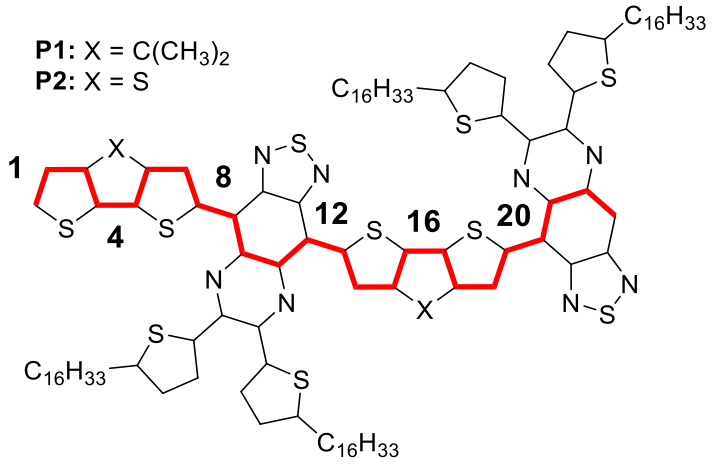

Bond Index	P1 Singlet	P2 Singlet	Bond Index	P1 Singlet	P2 Singlet
1	1.3742	1.3683	**13**	1.4045	1.3957
2	1.4181	1.4224	**14**	1.3959	1.4018
3	1.3875	1.3962	**15**	1.3960	1.4005
4	1.4363	1.4172	**16**	1.4261	1.4111
5	1.3901	1.3953	**17**	1.3961	1.4000
6	1.3998	1.4060	**18**	1.3959	1.4027
7	1.4018	1.3932	**19**	1.4039	1.3948
8	1.4447	1.4493	**20**	1.4445	1.4499
9	1.4228	1.4195	**21**	1.4244	1.4206
10	1.4533	1.4532	**22**	1.4512	1.4641
11	1.4292	1.4262	**23**	1.3872	1.4048
12	1.4458	1.4500			

Table S9. Tabulated bond length values (Å) of the tetramer (*n* = 4)

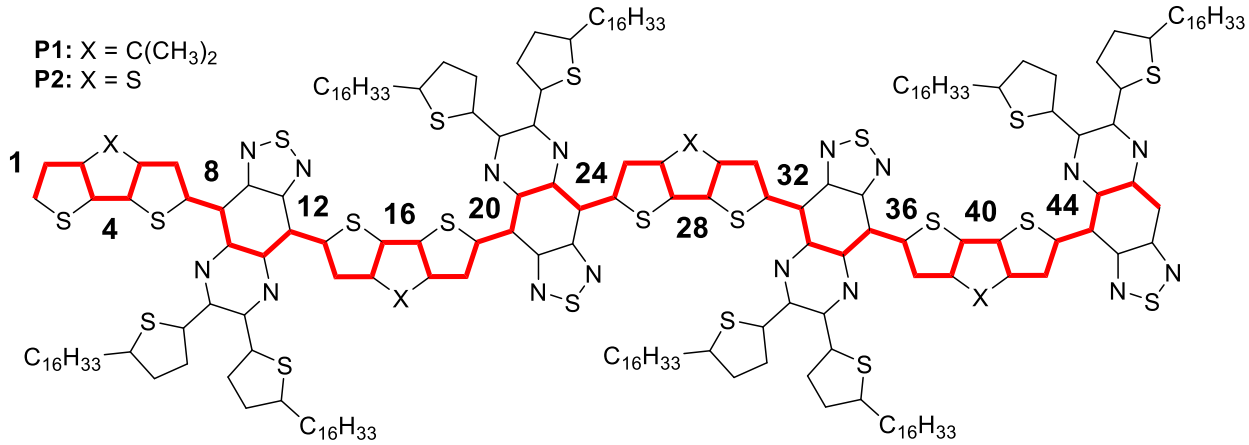

Bond Index	P1 Singlet	P2 Singlet	Bond Index	P1 Singlet	P2 Singlet	Bond Index	P1 Singlet	P2 Singlet	Bond Index	P1 Singlet	P2 Singlet
1	1.3747	1.3683	**13**	1.4196	1.3972	**25**	1.4240	1.3980	**37**	1.4159	1.3967
2	1.4173	1.4224	**14**	1.3814	1.4002	**26**	1.3780	1.3996	**38**	1.3864	1.4011
3	1.3891	1.3963	**15**	1.4113	1.4019	**27**	1.4143	1.4023	**39**	1.4046	1.4009
4	1.4336	1.4171	**16**	1.4050	1.4090	**28**	1.4022	1.4086	**40**	1.4162	1.4105
5	1.3931	1.3953	**17**	1.4124	1.4016	**29**	1.4138	1.4019	**41**	1.4027	1.4004
6	1.3962	1.4059	**18**	1.3801	1.4004	**30**	1.3793	1.4001	**42**	1.3906	1.4023
7	1.4073	1.3934	**19**	1.4231	1.3982	**31**	1.4232	1.3984	**43**	1.4092	1.3952
8	1.4366	1.4490	**20**	1.4192	1.4446	**32**	1.4199	1.4445	**44**	1.4388	1.4495
9	1.4329	1.4198	**21**	1.4431	1.4227	**33**	1.4412	1.4226	**45**	1.4284	1.4209
10	1.4489	1.4530	**22**	1.4450	1.4521	**34**	1.4462	1.4522	**46**	1.4497	1.4513
11	1.4456	1.4273	**23**	1.4523	1.4287	**35**	1.4466	1.4277	**47**	1.3897	1.3868
12	1.4265	1.4483	**24**	1.4198	1.4471	**36**	1.4294	1.4487			

Table S10. Tabulated bond length values (Å) of the hexamer (*n* = 6)

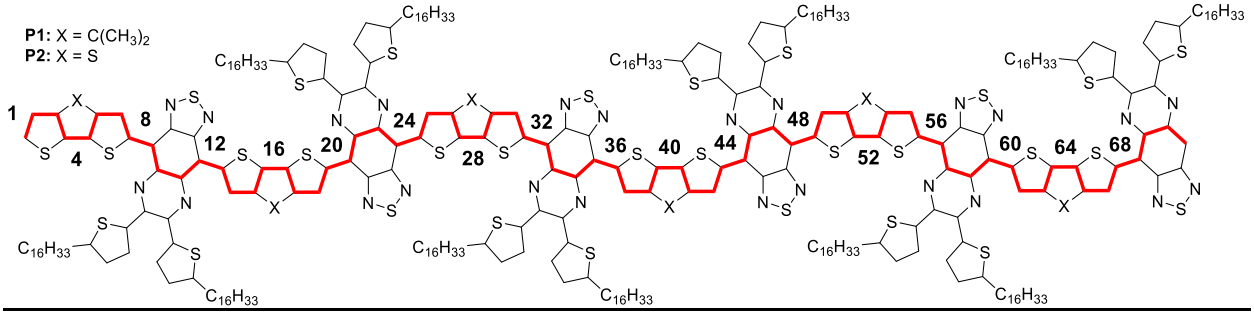

Bond Index	P1 Triplet	P2 Singlet	Bond Index	P1 Triplet	P2 Singlet	Bond Index	P1 Triplet	P2 Singlet
1	1.3749	1.3684	**25**	1.4348	1.3984	**49**	1.4327	1.3983
2	1.4170	1.4224	**26**	1.3683	1.3992	**50**	1.3707	1.3994
3	1.3896	1.3963	**27**	1.4259	1.4026	**51**	1.4224	1.4024
4	1.4328	1.4171	**28**	1.3872	1.4081	**52**	1.3926	1.4083
5	1.3941	1.3953	**29**	1.4265	1.4022	**53**	1.4212	1.4021
6	1.3950	1.4059	**30**	1.3681	1.3997	**54**	1.3732	1.4000
7	1.4089	1.3934	**31**	1.4367	1.3989	**55**	1.4301	1.3986
8	1.4342	1.4490	**32**	1.4033	1.4438	**56**	1.4120	1.4443
9	1.4358	1.4199	**33**	1.4536	1.4232	**57**	1.4464	1.4227
10	1.4476	1.4530	**34**	1.4405	1.4519	**58**	1.4441	1.4522
11	1.4503	1.4276	**35**	1.4640	1.4292	**59**	1.4442	1.4278
12	1.4202	1.4482	**36**	1.4043	1.4465	**60**	1.4243	1.4486
13	1.4248	1.3973	**37**	1.4369	1.3984	**61**	1.4195	1.3967
14	1.3766	1.4001	**38**	1.3669	1.3991	**62**	1.3835	1.4011
15	1.4168	1.4020	**39**	1.4273	1.4027	**63**	1.4075	1.4010
16	1.3977	1.4090	**40**	1.3859	1.4081	**64**	1.4130	1.4105
17	1.4186	1.4017	**41**	1.4271	1.4023	**65**	1.4048	1.4005
18	1.3745	1.4003	**42**	1.3679	1.3996	**66**	1.3889	1.4022
19	1.4299	1.3983	**43**	1.4368	1.3989	**67**	1.4109	1.3953
20	1.4107	1.4444	**44**	1.4037	1.4438	**68**	1.4370	1.4494
21	1.4497	1.4228	**45**	1.4528	1.4232	**69**	1.4481	1.4209
22	1.4421	1.4521	**46**	1.4411	1.4520	**70**	1.4650	1.4513
23	1.4614	1.4291	**47**	1.4616	1.4291	**71**	1.3905	1.3868
24	1.4070	1.4467	**48**	1.4086	1.4468			

Table S11. Tabulated bond length values (Å) of the octamer (*n* = 8)

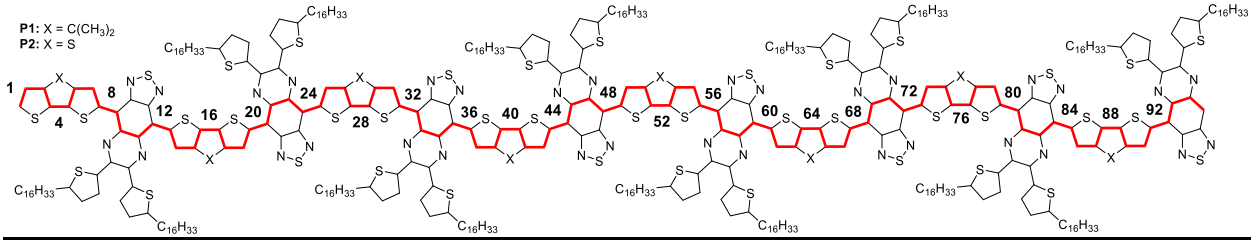

Bond Index	P1 Triplet	P2 Singlet	Bond Index	P1 Triplet	P2 Singlet	Bond Index	P1 Triplet	P2 Singlet
1	1.3748	1.3684	**33**	1.4526	1.4232	**65**	1.4256	1.4024
2	1.4171	1.4224	**34**	1.4410	1.4519	**66**	1.3691	1.3996
3	1.3895	1.3963	**35**	1.4631	1.4293	**67**	1.4353	1.3990
4	1.4330	1.4171	**36**	1.4051	1.4465	**68**	1.4055	1.4436
5	1.3938	1.3953	**37**	1.4363	1.3985	**69**	1.4515	1.4234
6	1.3953	1.4059	**38**	1.3672	1.3990	**70**	1.4415	1.4520
7	1.4086	1.3934	**39**	1.4270	1.4027	**71**	1.4487	1.4292
8	1.4347	1.4490	**40**	1.3859	1.4080	**72**	1.4104	1.4468
9	1.4353	1.4199	**41**	1.4273	1.4024	**73**	1.4313	1.3983
10	1.4479	1.4530	**42**	1.3675	1.3996	**74**	1.3720	1.3993
11	1.4494	1.4275	**43**	1.4374	1.3990	**75**	1.4210	1.4024
12	1.4215	1.4482	**44**	1.4027	1.4436	**76**	1.3944	1.4083
13	1.4238	1.3973	**45**	1.4538	1.4234	**77**	1.4198	1.4021
14	1.3775	1.4001	**46**	1.4405	1.4519	**78**	1.3743	1.3999
15	1.4157	1.4020	**47**	1.4639	1.4294	**79**	1.4288	1.3986
16	1.3991	1.4090	**48**	1.4042	1.4464	**80**	1.4135	1.4442
17	1.4175	1.4016	**49**	1.4369	1.3985	**81**	1.4454	1.4228
18	1.3755	1.4003	**50**	1.3668	1.3990	**82**	1.4445	1.4522
19	1.4287	1.3983	**51**	1.4274	1.4028	**83**	1.4438	1.4278
20	1.4122	1.4445	**52**	1.3856	1.4080	**84**	1.4253	1.4487
21	1.4486	1.4228	**53**	1.4275	1.4024	**85**	1.4188	1.3967
22	1.4426	1.4520	**54**	1.3674	1.3995	**86**	1.3840	1.4011
23	1.4599	1.4291	**55**	1.4373	1.3990	**87**	1.4069	1.4009
24	1.4090	1.4467	**56**	1.4029	1.4436	**88**	1.4136	1.4105
25	1.4332	1.3984	**57**	1.4535	1.4234	**89**	1.4044	1.4005
26	1.3697	1.3992	**58**	1.4406	1.4520	**90**	1.3892	1.4022
27	1.4242	1.4026	**59**	1.4503	1.4295	**91**	1.4106	1.3953
28	1.3892	1.4082	**60**	1.4055	1.4465	**92**	1.4374	1.4494
29	1.4249	1.4023	**61**	1.4357	1.3986	**93**	1.4295	1.4210
30	1.3694	1.3997	**62**	1.3680	1.3991	**94**	1.4493	1.4513
31	1.4352	1.3989	**63**	1.4259	1.4027	**95**	1.3903	1.3868
32	1.4050	1.4438	**64**	1.3876	1.4080			

Table S12. A review of open-shell radical species reported half-life times

Reference	*Year*	*Compound*	*Half-life*	*Conditions*
12	2011	**16**	60 min	solution, air, dark
13	2012	**1-OS**	495 min	solution
14	2013	**3a**	900 min	solution, air, light
15	2014	**1a**	7 days	solution, air, dark
15	2014	**1b**	3.5 days	solution, air, dark
15	2014	**1c**	43 days	solution, air, dark
16	2021	**4**	6.5 days	solution, air, light
17	2021	**4-PA**	180 min	solution, air, light
17	2021	**7-PA**	25 min	solution, inert
18	2021	**8**	19 days	solution, inert
18	2021	**16**	420 min	solution, inert

6. Supplemental references

1. Wang, M., Ford, M.J., Zhou, C., Seifrid, M., Nguyen, T.-Q., and Bazan, G.C. (2017). Linear conjugated polymer backbones improve alignment in nanogroove-assisted organic field-effect transistors. J. Am. Chem. Soc. *139*, 17624-17631. 10.1021/jacs.7b10332.
2. Kini, G.P., Lee, S.K., Shin, W.S., Moon, S.-J., Song, C.E., and Lee, J.-C. (2016). Achieving a solar power conversion efficiency exceeding 9% by modifying the structure of a simple, inexpensive and highly scalable polymer. J. Mater. Chem. A *4*, 18585-18597. 10.1039/C6TA08356K.
3. Miyaji, T., Tsubota, Y., Suzuki, T., Yamashita, Y., Mukai, T., and Miyashi, T. (1992). Tetracyanoquinodimethanes fused with 1,2,5-thiadiazole and pyrazine units. Heterocycles *33*, 337-348. 10.3987/com-91-s44.
4. Richter, T.V., Braun, C.H., Link, S., Scheuble, M., Crossland, E.J.W., Stelzl, F., Würfel, U., and Ludwigs, S. (2012). Regioregular polythiophenes with alkylthiophene side chains. Macromolecules *45*, 5782-5788. 10.1021/ma2026644.
5. Huang, L., Eedugurala, N., Benasco, A., Zhang, S., Mayer, K.S., Adams, D.J., Fowler, B., Lockart, M.M., Saghayezhian, M., Tahir, H., et al. (2020). Open-shell donor–acceptor conjugated polymers with high electrical conductivity. Adv. Funct. Mater. *30*, 1909805. 10.1002/adfm.201909805.
6. Bleaney, B., and Bowers, K.D. (1952). Anomalous paramagnetism of copper acetate. Proc. R. Soc. London, Ser. A *214*, 451-465. 10.1098/rspa.1952.0181.
7. Y. D. Tsvetkov, M.K.B., Y. Grishin, A. (2019). Pulsed Electron-Electron Double Resonance: Nanoscale Distance Measurement in the Biological, Materials and Chemical Sciences (Springer International Publishing).
8. Morgan, G.G., and Kühne, I.A. (2020). Practical Approaches to Biological Inorganic Chemistry (Second Edition), 2nd Edition (Elsevier). 10.1016/B978-0-444-64225-7.00003-1.
9. Becke, A.D. (1993). A new mixing of Hartree–Fock and local density-functional theories. J. Chem. Phys. *98*, 1372-1377. 10.1063/1.464304.
10. Chen, Z., Wannere, C.S., Corminboeuf, C., Puchta, R., and Schleyer, P.v.R. (2005). Nucleus-independent chemical shifts (NICS) as an aromaticity criterion. Chem. Rev. *105*, 3842-3888. 10.1021/cr030088+.
11. Yamaguchi, K., Fukui, H., and Fueno, T. (1986). Molecular orbital (MO) theory for magnetically interacting organic compounds. Ab-initio MO calculations of the effective exchange integrals for cyclophane-type carbene dimers. Chem. Lett. *15*, 625-628. 10.1246/cl.1986.625.
12. Kubo, T., Katada, Y., Shimizu, A., Hirao, Y., Sato, K., Takui, T., Uruichi, M., Yakushi, K., and Haddon, R.C. (2011). Synthesis, crystal structure, and physical properties of sterically unprotected hydrocarbon radicals. J. Am. Chem. Soc. *133*, 14240-14243. 10.1021/ja2065768.
13. Zeng, Z., Sung, Y.M., Bao, N., Tan, D., Lee, R., Zafra, J.L., Lee, B.S., Ishida, M., Ding, J., López Navarrete, J.T., et al. (2012). Stable Tetrabenzo-Chichibabin's hydrocarbons: tunable ground

state and unusual transition between their closed-shell and open-shell resonance forms. J. Am. Chem. Soc. *134*, 14513-14525. 10.1021/ja3050579.

14. Konishi, A., Hirao, Y., Matsumoto, K., Kurata, H., Kishi, R., Shigeta, Y., Nakano, M., Tokunaga, K., Kamada, K., and Kubo, T. (2013). Synthesis and characterization of quarteranthene: elucidating the characteristics of the edge state of graphene nanoribbons at the molecular level. J. Am. Chem. Soc. *135*, 1430-1437. 10.1021/ja309599m.
15. Tian, Y., Uchida, K., Kurata, H., Hirao, Y., Nishiuchi, T., and Kubo, T. (2014). Design and synthesis of new stable fluorenyl-based radicals. J. Am. Chem. Soc. *136*, 12784-12793. 10.1021/ja507005c.
16. Shen, J.-J., Han, Y., Dong, S., Phan, H., Herng, T.S., Xu, T., Ding, J., and Chi, C. (2021). A stable [4,3]peri-acene diradicaloid: synthesis, structure, and electronic properties. Angew. Chem., Int. Ed. *60*, 4464-4469. 10.1002/anie.202012328.
17. Ajayakumar, M.R., Ma, J., Lucotti, A., Schellhammer, K.S., Serra, G., Dmitrieva, E., Rosenkranz, M., Komber, H., Liu, J., Ortmann, F., et al. (2021). Persistent peri-heptacene: synthesis and in-situ characterization. Angew. Chem., Int. Ed. *n/a*. 10.1002/anie.202102757.
18. Chen, Q., Baumgarten, M., Wagner, M., Hu, Y., Hou, I.C.-Y., Narita, A., and Müllen, K. (2021). Dicyclopentaannelated hexa-peri-hexabenzocoronenes with a singlet biradical ground state. Angew. Chem., Int. Ed. *60*, 11300-11304. 10.1002/anie.202102932.